Exploring vegetation impact on near-road aerosol

- By simulations using the $k-\epsilon$ turbulence model -

Boris Bremmers
4443624

To obtain the degree BSc Applied Physics at the Delft University of Technology, to be defended publicly on Thursday August 23, 2018 at 9:30 a.m.

TU Delft

Committee:
Dr.ir. D.A. Vermaas
Dr. S. Kenjereš, Dipl.-Ing.

Bachelor Thesis
Delft University of Technology

Delft, August 17, 2018
Supervisor: Dr. S. Kenjereš

Contents

Abstract

Air pollution within cities is rising; PM levels are estimated to have increased with 8% in the past five years [WHO, 2016]. Although rapidly emerging technological advancements appear to provide the answer, deterioration of air quality is only expected to increase in the future as world population is growing [Vidal, 2016]. Roadside vegetation barriers are assessed as part of a potential solution to this rising problem. In this study, a $k-\epsilon$ turbulence model [Kenjereš and Ter Kuile, 2013] including a dry deposition model, describing dispersion and deposition processes experienced by the particles [Petroff et al., 2008], is compared with a large eddy simulation (LES) turbulence model [Tong et al., 2016]. To do so, a model describing the leaf area density (LAD) is created first. Furthermore, the performance of the simulation model itself is validated with experimental data [Tiwary et al., 2006] as well as previously run simulations [Tierolff, 2018]. Next, a vegetation barrier is employed to explore its effects on particle concentrations released from a highway emission zone located upwind of it. Results show a significant decrease in downwind particle concentration, but do not display a realistic concentration profile. In conclusion, this study was unable to provide similar results as those obtained by Tong et al., [2016]. After more realistic results are obtained using nano-sized particles, relevant information could be provided for urban planning and developing infrastructure by imitating desirable real-life barrier configurations.

1 Preface

Although awareness of air pollution within cities is rising and rapidly emerging technological advancements appear to provide the answer, PM levels are estimated to have increased with 8% in the past five years [WHO, 2016]. Furthermore, deterioration of air quality is only expected to increase in the future, as world population is growing [Vidal, 2016]. The inhalable aerosol is composed of a complex mixture of tiny particles ($\leq \mathrm{PM}_{10}$), such as sulphate, nitrates, ammonia, sodium chloride, black carbon, mineral dust and water, suspended in air [WHO, 2018]; hence they are invisible to the naked eye and therefore can be of insidious danger.

In this research, roadside vegetation barriers are assessed as a potential solution to polluted air. A $k-\epsilon$ turbulence model [Kenjereš and Ter Kuile, 2013] including a dry deposition model, describing dispersion and deposition processes experienced by the particles [Petroff et al., 2008], is compared with a large eddy simulation (LES) turbulence model [Tong et al., 2016]. The main objective of this study is to compare and evaluate results, obtained by the time-independent RANS solver, to those provided by Tong et al., [2016], which uses the more complicated LES model instead. Simulation specifications are matched to those used in the case study. Furthermore, this study endeavours to contribute to research that investigates their points of resemblance and difference.

Section 2 consists of theory, describing RANS together with the $k-\epsilon$ turbulence closure model as well as the transport of pollution. Moreover, modelling the leaf area density (LAD) and the use of a differencing scheme are explained.

Section 3 presents the results together with discussion. In the first two subsections, the LAD model and the performance of the simulation model are validated. Subsection three shows the results that are compared to data retrieved from Tong [2016].

This research is executed on behalf of the BSc thesis report belonging to the bachelor Applied Physics of Delft University of Technology.

2 Theoretical Background

Navier-Stokes theory sets the basis for Computational Fluid Dynamics (CFD) and is worth taking a look at beforehand. The equations were first developed by Navier in France in 1822 using molecular arguments [Bird et al., 1962]. However, besides the analytically absolute equations developed by Navier, Reynolds made his own variant of them, essential for CFD to function.

2.1 Equation of motion

From a mass balance over a stationary and infinite small volume element, the so-called equation of continuity can be derived:

$$\frac{\partial \rho}{\partial t} + \frac{\partial}{\partial x_i}(\rho U_i) = 0 \tag{2.1–1}$$

The equation, which describes nothing more than the conservation of mass, comes with an important implication. Namely, when considering an incompressible fluid, meaning $\rho =$ constant, the following conclusion can be drawn: $\partial U_i / \partial x_i = 0$.

Now, performing a momentum balance in a similar way as was done for the mass balance, one can derive the equation of motion and from that the sought Navier-Stokes equations. These equations are therefore nothing more but equations for the conservation of momentum. Momentum passes the volume element by two mechanisms: by convection and by molecular transfer. Convection is represented by simply the rate of the bulk fluid flow whereas molecular transfer by stress terms [Bird et al., 1962]. Moreover, in contrast to mass, momentum can be produced inside the volume element due to external forces acting on the system. The stress terms together form a second-order tensor and can be rewritten into two parts; one part that corresponds to the average stress in all directions, that is, the hydrostatic pressure P, and a part in which the stresses are determined by other viscous effects.

The general form of the Navier-Stokes equations with varying density and viscosity follows:

$$\rho\left(\frac{\partial U_i}{\partial t} + U_j \frac{\partial U_i}{\partial x_j}\right) = -\frac{\partial P}{\partial x_i} + \frac{\partial}{\partial x_j}\mu\left(\frac{\partial U_i}{\partial x_j} + \frac{\partial U_j}{\partial x_i}\right) - \frac{2}{3}\frac{\partial}{\partial x_i}\mu\frac{\partial U_j}{\partial x_j} + F_i \tag{2.1–2}$$

In this equation, μ is defined as the dynamic viscosity of the fluid. The Navier-Stokes equations as expressed above, are rarely used in physics when performing calculation, as they are usually simplified making use of specific conditions [Hinze, 1959]. For example, equation (2.1–2) will be simplified when the viscosity of the fluid can be assumed to be constant, as is the case in this research. The second term on the right-hand side of equation can then be rewritten and the general expression for the Navier-Stokes equations is modified to:

$$\rho\left(\frac{\partial U_i}{\partial t} + U_j \frac{\partial U_i}{\partial x_j}\right) = -\frac{\partial P}{\partial x_i} + \mu\frac{\partial^2}{\partial {x_j}^2}U_i + \frac{1}{3}\mu\frac{\partial U_j}{\partial x_i \partial x_j} + F_i \tag{2.1–3}$$

2.2 Reynolds averaged

In order to be able to perform computational calculations on equation (2.1–3), it has to be adjusted by separating the three terms U, ρ and P in an average and fluctuating part. These terms to be substituted, look as follows:

$$U_i = \bar{U}_i + u_i \qquad \rho = \bar{\rho} + \tilde{\rho} \qquad P = \bar{P} + p \tag{2.2–1}$$

The average part is defined as $\bar{A} = 1/T \int_0^T A(t+\tau)d\tau$, with T large compared to the time scale of the turbulent motions. Important to realize is that the average of the fluctuating part equals zero, thus: $\bar{a} = 0$; for the average of the average part, on the other hand, applies: $\bar{\bar{A}} = \bar{A}$, while the average of two different fluctuating parts will also not result in zero, so: $\overline{ab} \neq 0$. With these characteristics in mind, the three expression given by equation (2.2–1) must be substituted in the Navier-Stokes equation of a fluid with constant viscosity (2.1–3) and overall averaged with respect to time, resulting in three correlations of turbulence: $\overline{u_i u_j}$, $\overline{\tilde{\rho} u_i}$ and $\overline{\tilde{\rho} u_i u_j}$. In this study the effect of compressibility may be neglected, as is usual for most studies considering turbulent motion. This second assumption implies that $\tilde{\rho}$ is negligibly small and hence $\rho = \bar{\rho} = \textit{Constant}$. Furthermore, applying a constant density to equation (2.1–1), results in: $\partial U_j/\partial x_j = 0 = \partial \bar{U}_j/\partial x_j = \partial u_j/\partial x_j$. Only one turbulence term will remain and equation (2.1–3) can ultimately be written as:

$$\rho\left(\frac{\partial \bar{U}_i}{\partial t} + \bar{U}_j \frac{\partial \bar{U}_i}{\partial x_j}\right) = -\frac{\partial \bar{P}}{\partial x_i} + \frac{\partial}{\partial x_j}\left(\mu \frac{\partial \bar{U}_i}{\partial x_j} - \rho \overline{u_i u_j}\right) + \bar{F}_i \tag{2.2–2}$$

The remaining turbulence term is thus $\overline{u_i u_j}$, which can be interpreted as an additional stress. These turbulence stresses $\rho\overline{u_i u_j}$ are referred to as Reynolds stresses, because Reynolds was the first to write the general expression for the Navier-Stokes equations, equation (2.1–2), in the form of equation (2.2–2) [Hinze, 1959], suitably known as the Reynolds-averaged Navier-Stokes equation (RANS).

Furthermore, in this research the term representing external forces acting on the fluid $\bar{F}_i$, is a drag force due to vegetation and will be discussed together with the source/sink terms in subsection 2.4.

2.3 Turbulence closure model $k-\epsilon$

The Reynolds stresses are in fact an unknown second order tensor, existing of nine components. It could be assumed that these turbulence stresses act like viscous stresses, such that they are directly proportional to the mean velocity gradient, which was first proposed by Boussinesq [Hinze, 1959]. He introduced a so-called eddy or turbulence viscosity, ν_t, as scalar, from which the subsequent relation for the turbulence stresses follow:

$$-\overline{u_i u_j} = \nu_t\left(\frac{\partial U_i}{\partial x_j} + \frac{\partial U_j}{\partial x_i}\right) - \frac{2}{3}k\delta_{ij} \tag{2.3–1}$$

Here k is the turbulent kinetic energy and represents the normal-stress components which are obtained when putting $i{=}j$ for the turbulence stresses and hence is defined as: $k \equiv \overline{u_i^2}/2$. In the $k-\epsilon$ turbulence model, the eddy viscosity is appropriately modelled by the variables $k-\epsilon$ according to:

$$\nu_t = C_\mu k^2/\epsilon \tag{2.3–2}$$

The parameter C_μ is a model constant, whereas ϵ is a dependent variable and represents the rate of dissipation of the turbulence kinetic energy, k. When the assumption can be made that the dissipating eddies are isotropic, ϵ is defined as: $\epsilon \equiv \nu\overline{(\partial u_i/\partial x_j)^2}$, with $\nu = \mu/\rho$, representing the kinematic viscosity [Bradshaw et al., 1981].

To close the model, two modelled partial differential transport equations (PDE's) describing both k and ϵ need to be solved. To be able to derive these equations, the RANS equation (2.2–2) needs to be slightly adjusted by subtracting it from the Navier-Stokes equations for incompressible fluids, looking back at the general expression for these equations given by formula (2.1–2). The transport equation for the velocity fluctuation u_i then follows and reads:

$$\frac{\partial u_i}{\partial t} + \bar{U}_j \frac{\partial u_i}{\partial x_j} = -\frac{1}{\rho}\frac{\partial p}{\partial x_i} + \frac{\partial}{\partial x_j}\left(\nu \frac{\partial u_i}{\partial x_j} + \overline{u_i u_j} - u_i u_j\right) - u_j \frac{\partial \bar{U}_i}{\partial x_j} + \frac{\tilde{f}_i}{\rho} \tag{2.3–3}$$

Furthermore, there is divided by ρ so that the viscosity is written in its kinematic form. From equation (2.3–3) and using the previously given definitions of k and ϵ, the modelled PDE's describing both these parameters can be derived.

To end up with the modelled k-equation, the transport equation for the velocity fluctuation (2.3–3) needs to be multiplied by u_i, averaged and finally modelled. The equation then reads:

$$\frac{\partial k}{\partial t} + \bar{U}_j \frac{\partial k}{\partial x_j} = \frac{\partial}{\partial x_j}\left[\left(\nu + \frac{\nu_t}{\sigma_k}\right)\frac{\partial k}{\partial x_j}\right] - \overline{u_i u_j}\frac{\partial \bar{U}_i}{\partial x_j} - \epsilon + S_k \tag{2.3–4}$$

The above equation (2.3–4) is the modelled form of the turbulent kinetic energy PDE, with σ_k the effective Prandtl-Schmidt number as model constant and S_k the source term relating k to tree effects [Tan, 2009]. In contrast to the predominantly exact derivation behind the k-equation, the ϵ-equation is more based on empiricism, which is shown by the extra modelling constants. The ϵ-equation can be derived by differentiating equation (2.3–3) with respect to x_j, then multiplying by $2\nu(\partial u_i/\partial x_j)$, subsequently averaging and finally modelling [Hanjalić et al., 2009]. The equation then reads:

$$\frac{\partial \epsilon}{\partial t} + \bar{U}_j \frac{\partial \epsilon}{\partial x_j} = \frac{\partial}{\partial x_j}\left[\left(\nu + \frac{\nu_t}{\sigma_\epsilon}\right)\frac{\partial \epsilon}{\partial x_j}\right] - C_{\epsilon 1}\overline{u_i u_j}\frac{\partial \bar{U}_i}{\partial x_j}\frac{\epsilon}{k} - C_{\epsilon 2}\frac{\epsilon^2}{k} + S_\epsilon \tag{2.3–5}$$

The above equation (2.3–5) is the modelled expression of the rate of k dissipation PDE, with σ_ϵ, $C_{\epsilon 1}$ and $C_{\epsilon 2}$ three new model constants and S_ϵ the sink term of ϵ [Tierolff, 2018].

2.4 Elaboration on drag, source and sink terms

The drag term $\bar{F}_i$ from the RANS equation (2.2–2), the source term S_k from equation (2.3–4) and the sink term S_ϵ from equation (2.3–5) are all representative of the way the vegetation affects the fluid flow. To start with, $\bar{F}_i$ is a drag term which the vegetation imposes on the air moving through its leaves and branches [Steffens et al., 2012]. Air hitting vegetation acts similar as it does with solid obstacles, causing large-scale turbulent motion to occur. The interaction of the air with the vegetation produces eddies behind the obstacle that are of equal size as a whole due to shear [Tierolff, 2018]. The momentum drag is proportional to the plant drag coefficient C_D and the leaf area density (LAD). The LAD is the ratio of leaf surface area to the total volume occupied by the vegetative element [Tong et al., 2016], thus in [m^2/m^3]. It is an essential parameter in order to characterize different kind of vegetation to perform calculations with and will be intensively used

throughout this report. The formula describing the relation between the drag force and these two parameters reads:

$$\bar{F}_i = -\frac{1}{2}\rho C_D \text{LAD} |\bar{U}| \bar{U}_i \tag{2.4–1}$$

As air moves through the vegetation's canopy, small branches as well as individual leaves disturb the mean fluid flow and convert kinetic energy to turbulent kinetic energy [Steffens et al., 2012]. Small sized eddies are produced with roughly the same size as the leaves themselves and are typified as wake turbulence. However, this turbulence created is quickly dissipated, meaning although the turbulence behind the canopy might be high, locally there is a low turbulence regime. The accelerated dissipation occurs because the small sized eddies allow for a shortcut in the turbulence cascade, a phenomenon unique to porous objects [Tierolff, 2018]. The turbulent kinetic energy is hence modelled as a combination of a source term S_k representing the creation of turbulent kinetic energy k and a sink term S_ϵ representing the rapid dissipation of eddies ϵ from k [Steffens et al., 2012]. The source term of k scales with the cube of the mean velocity and with k itself. The expression is given by:

$$S_k = \frac{1}{2} C_D \text{LAD} \left(\beta_p |\bar{U}|^3 - \beta_d |\bar{U}| k \right) \tag{2.4–2}$$

The term β_p represents the fraction of mean fluid flow converted to turbulent kinetic energy – production of k – and β_d represents the fraction of turbulent kinetic energy dissipated within the canopy – destruction of k – and are both model constants. With the help of dimensional analysis by making use of the characteristic time k/ϵ [s] and by adding new model constants, an expression for the sink term is composed from the source term equation (2.4–2) and reads:

$$S_\epsilon = \frac{1}{2} C_D \text{LAD} \left(C_{\epsilon 4} \beta_p \frac{\epsilon}{k} |\bar{U}|^3 - C_{\epsilon 5} \beta_d |\bar{U}| \epsilon \right) \tag{2.4–3}$$

Here $C_{\epsilon 4}$ and $C_{\epsilon 5}$ are model constants and regulate, together with β_p and β_d, the effectiveness the vegetation has on the fluid flow in the $k-\epsilon$ model [Kenjereš and Ter Kuile, 2013]. The constant β_p is equal to "1" for dense canopies, as is assumed in this research [Steffens et al., 2012]. A full list of all the model constants that are used to close the $k-\epsilon$ model and thereby solve the source and sink terms, is given below in tables 1 and 2:

C_μ	σ_k	σ_ϵ	$C_{\epsilon 1}$	$C_{\epsilon 2}$
0.09	1.0	1.3	1.44	1.92

Table 1: Closure model [Launder and Sharma, 1974]

β_p	β_d	$C_{\epsilon 4}$	$C_{\epsilon 5}$
1.0	5.1	0.9	0.9

Table 2: Source & sink terms [Katul et al., 2004]

2.5 Transport of pollution

Air pollution is caused by tiny particles, with sizes of $PM_{2.5}$ and lower posing the greatest health risk [WHO, 2018]. Their small sizes and the relatively low concentration they retain, allow for the $k-\epsilon$ model to still be considered completely valid. A transport equation for the concentration C of the polluting particles can therefore be drafted independently and shows similar characteristics to the RANS equation (2.2–2):

$$\frac{\partial \bar{C}}{\partial t} + \bar{U}_j \frac{\partial \bar{C}}{\partial x_j} = \frac{\partial}{\partial x_j} \left(D \frac{\partial \bar{C}}{\partial x_j} - \overline{c u_j} \right) + S_C \tag{2.5–1}$$

The term D is the diffusion coefficient and S_C the source/sink term related to concentration changes. The turbulence term $\overline{cu_j}$ can be modelled as:

$$\overline{cu_j} = -K\frac{\partial \bar{C}}{\partial x_j} \tag{2.5–2}$$

The term K is the eddy diffusion coefficient from which the turbulent Schmidt number is defined as: $\mathrm{Sc}_t = \nu_t/K$.

The source/sink term is determined by two separate processes, namely dry deposition on vegetation and gravitational settling, giving: $S_C = S_C^D + S_C^G$. The expression for the gravitational settling reads:

$$S_C^G = -\frac{\partial}{\partial x_i}\left(\bar{C}\bar{U}_{s,i}\right) \tag{2.5–3}$$

Logically, the settling velocity $\bar{U}_{s,i}$ only has a z-component because equation (2.5–3) concerns gravity. The settling velocity can be calculated from a force balance consisting of drag and gravitational forces. Furthermore, the Cunningham correction factor C_c needs to be added to account for non-continuum effects, as equation (2.5–3) regards small particles. The settling velocity is then given by:

$$\bar{U_s} = \frac{C_c g \rho_p {d_p}^2}{18\mu} \tag{2.5–4}$$

In equation (2.5–4), d_p is the diameter of the particle, ρ_p the particle's density, g the gravitational force and C_c the already mentioned Cunningham correction factor. This correction factor is approximated by: $C_c = 1 + 3.334\frac{\lambda}{d_p}$, with λ the mean free path of the particle having a value of 0.066μm. The approximated expression for C_c allows the numerical simulation to run smoother. On the given size interval of the particles the maximum difference is 12%.

An expression for the second process, namely the dry deposition of the polluting particles, is given by:

$$S_C^D = -\mathrm{LAD}\bar{U}_k\bar{C} \tag{2.5–5}$$

The term $\bar{U}_k$ represents the average deposition velocity, with the subscript k indicating the deposition process, like:

- Brownian diffusion – The irregular movement of aerosol suspended in air, caused by collisions between the particles and surrounding molecules of much smaller size. Affects mostly smaller particles with diameter $d_p < 0.1\mu$m.
- Interception – Occurs when a particle passing the obstacle too close, gets captured on it.
- Sedimentation – Happens when aerosol collides with the obstacle due to the downward motion of the particle cause by the gravitational force. Affects mostly larger particles with diameter $d_p > 10\mu$m.
- Impaction – Takes place when a particle, which does not follow the streamline due to its inertia, collides with the obstacle and can have an inertial or turbulent origin.

These all are a function of d_p and hence follows: $\bar{U}_k(d_p) = f(\bar{U}_{Br}, \bar{U}_{In}, \bar{U}_{Se}, \bar{U}_{T.Im}, \bar{U}_{I.Im})$ [Šíp and Beneš, 2016]. Furthermore, there needs to be made distinction between two different types of collectors when treating deposition processes, namely needle-like collectors

and broadleaved collectors. To be able to write an expression for $\bar{U}_k$ in equation (2.5–5), an elementary deposition velocity u_k, acting on a single leaf, is defined. Moreover, two assumptions have to be made in order to determine the collective deposition in a given reference volume D_{ref}.

First of all, any of the individual deposits is a function of the area of a single leaf s as well as of $\Psi_k = \{s, \psi_{k,1}, ..., \psi_{k,q}\}$, describing the q physical quantities which defines the deposit influencing factors, such as vegetation element specifications and aerodynamics. An relationship for the individual deposits and the elementary deposition velocity can then be written as:

$$d_k(\boldsymbol{M}, t, \Psi_k) = -s\bar{C}u_k(\boldsymbol{M}, t, \Psi_k) \tag{2.5–6}$$

With $\boldsymbol{M}$ defined as a point on the interface between the vegetation and the air containing aerosols.

Secondly, the number of leaves within the reference volume is assumed to be large enough to define a joint probability density function (pdf), $\phi(\boldsymbol{M}, t, \Psi_k)$, of s and Ψ_k, which corresponds to the deposition process k under consideration. Using the one-dimensional pdf $\phi_s(\boldsymbol{M}, s)$, the LAD can be derived by: $\text{LAD}(\boldsymbol{M}) = C_{\text{N}}(\boldsymbol{M})\bar{s}(\boldsymbol{M})$, with C_{N} the number of vegetation elements per unit volume and $\bar{s}$ the average surface of the leaves inside the reference volume D_{ref}. An expression for the average deposition velocity can now be defined and is given by:

$$\bar{U}_k = \int_{D_{\text{ref}(\Psi_k)}} \frac{s}{\bar{s}} u_k \phi \delta \Psi_k \tag{2.5–7}$$

Equation (2.5–7) can be substituted in equation (2.5–5) to determine the concentration sink term due to dry deposition [Petroff et al., 2008].

2.6 LAD modelling

The leaf area density has already been briefly mentioned in subsection 2.4, where its importance in this research was emphasized. The LAD is the all decisive factor when computing interaction between polluting particles and vegetation. It is a function of the height z, depends on tree species and is a quite difficult quantity to measure inside a forest canopy. Because of this reason, the ability to describe the LAD realistically using an empirical relationship would be extremely powerful.

Three parameters are needed in this model, namely the tree height h, the maximum value of the leaf area density L_m and corresponding height z_m. Watching the morphological nature of trees, two conditions the formula should meet are imposed:

I. When $z \to 0$ and $z \to h$, then $\text{LAD}(z)$ must tend to zero.

II. At $z = z_m$, $\text{LAD}(z)$ should have its maximum, that is, $L_m = \text{LAD}(z_m)$.

In deducing the empirical relationship for the LAD, it is assumed that the formula has a linear tendency for $z \geq z_m$, while it shows a hyperbolic behavior for $z < z_m$. To implement this assumption into the final formula, a parameter n is introduced, with two values corresponding to these two intervals. With the help of eight datasets which include the parameters as well as measured values of the LAD, derived from four different types of forest, the two values of n could be determined. Analysis of minimum root-mean-square

error trying different values of n and comparing the results with the datasets gave the following values:

$$n = \begin{cases} 6, & 0 \leq z < z_m \\ \frac{1}{2}, & z_m \leq z \leq h \end{cases} \tag{2.6–1}$$

The empirical model describing LAD(z) is derived using a mathematical procedure established by Planck, which he used to discover the formula for pure-temperature radiation, reading:

$$\mathrm{LAD}(z) = L_m \left(\frac{h - z_m}{h - z} \right)^n \exp\left[n \left(1 - \frac{h - z_m}{h - z} \right) \right] \tag{2.6–2}$$

With the values of n, as given in equation (2.6–1), to be substituted for the given intervals [Lalic and Mihailovic, 2004]. The parameter h can straightforwardly be measured while z_m can be divided into three groups corresponding to different types of trees: 1) $z_m = 0.8h$ (oak and silver birch), 2) $0.6h < z_m < 0.8h$ (common maple), and 3) $z_m = 0.6h$ (pine), with typical species written in the brackets [Kolic, 1978]. This leaves one still to be discussed parameter L_m. Although in some cases L_m is a known parameter, most of the times it is not. The leaf area index (LAI) – defined by the ratio of the leaf surface area to the ground surface area [Tong et al., 2016], thus with unit [$\mathrm{m}^2/\mathrm{m}^2$] – provides a solution, due to its analytical relationship with the LAD, given by:

$$\mathrm{LAI} = \int_0^h \mathrm{LAD}(z) dz \tag{2.6–3}$$

When the LAI is known, L_m can be calculated by numerically integrating equation (2.6–3). In essence, the parameter L_m, needed for this model, is changed to a new parameter LAI from which L_m indirectly follows. The LAI can be measured, in contrast to L_m, using specific equipment such as the LAI-2000 plant canopy analyzer [Hagler et al., 2012].

After the LAD profile of a given canopy is calculated, it may be discretized in a preferable number of bins. With each obstacle block in the z-direction, a corresponding value of the LAD exists. In figure 1 below, an example is given with 10 bins of such a discretized LAD profile, calculated using the theory from this subsection:

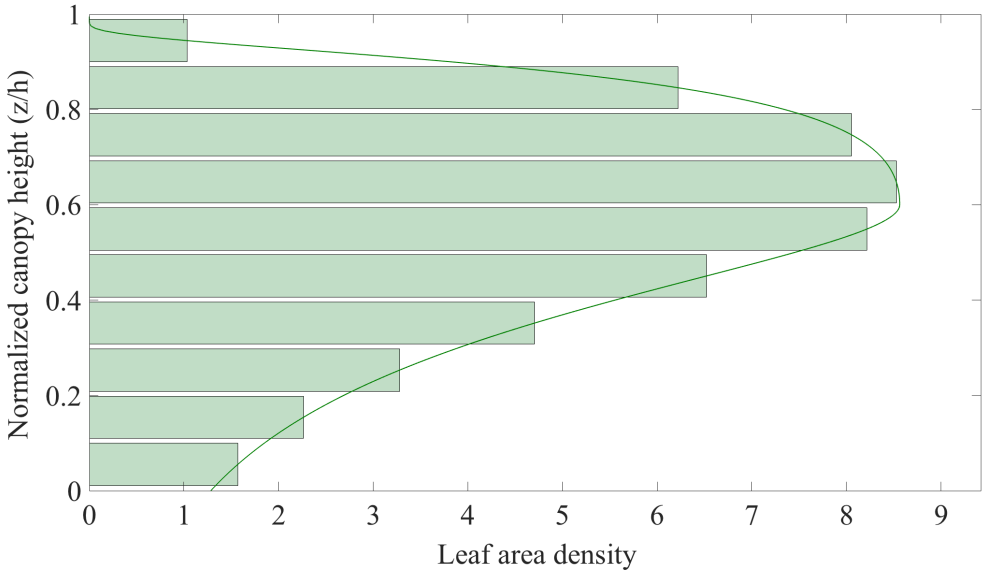

Figure 1: Calculated LAD profile divided into 10 horizontal bins. The LAD is normalized by multiplying by the canopy height.

To calculate this particular LAD profile, the following three parameters were used: $h = 20$m, $z_m = 0.6h$ and LAI $= 5$. It represents a pine tree and was used in an experiment with which results of the model are compared in subsection 3.1 [Shaw and Schumann, 1992]. Figure 2 below shows the same LAD profile but then divided by 20 bins. One can expect that when the number of bins increases, the analytically calculated LAD profile is approached more accurately.

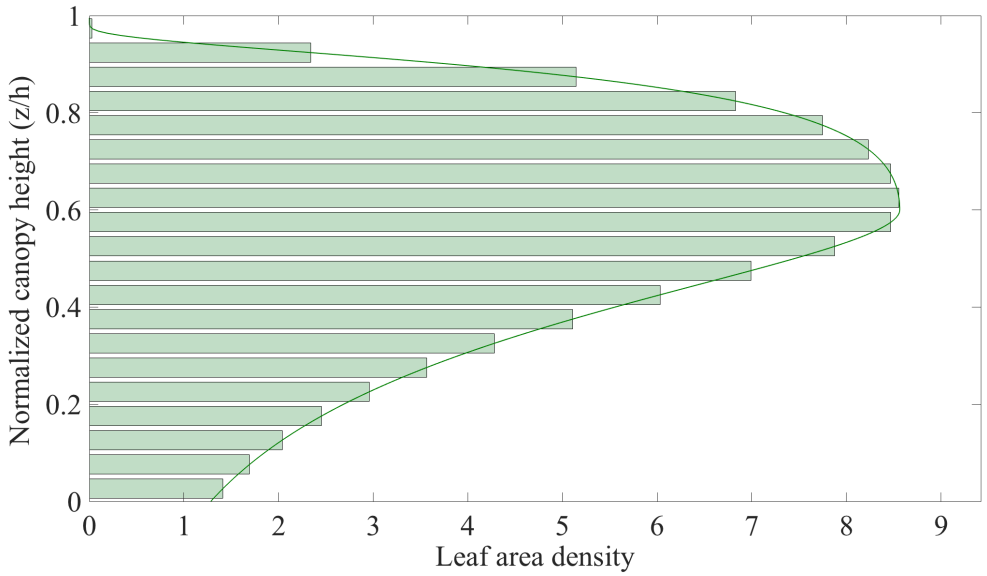

Figure 2: Calculated normalized LAD profile divided into 20 horizontal bins.

2.7 Differencing scheme

In order to perform numerical simulations, a differencing scheme must be applied. A space is divided into a given number of control volumes and for each of these control volumes, a value is calculated using the transport equations. The differencing scheme is then used to assign cell face values of a control volume based on the values the surrounding control volumes have. The quadratic upwind differencing scheme (QUDS) fits a quadratic function through three separate points, two of which surround the cell face and one which is located on the upstream side. Illustration 3 below shows an one-dimensional example:

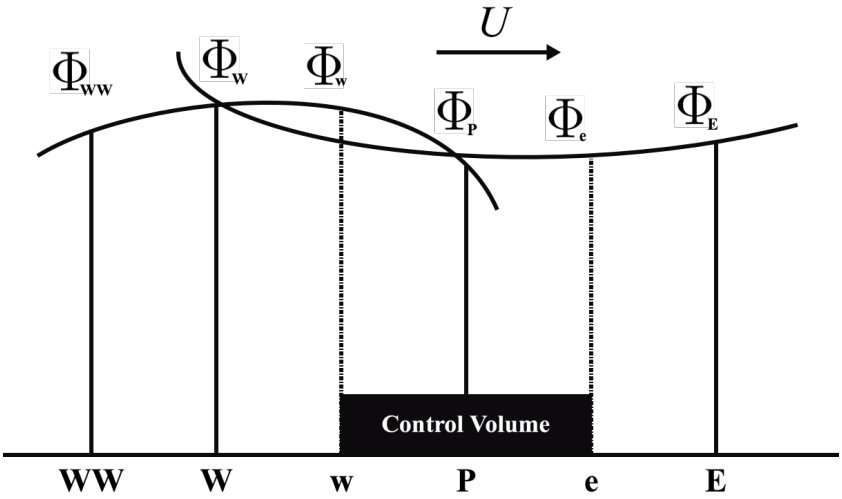

Figure 3: One-dimensional QUDS example.

Point **P** represents the center of a given control volume with points **w** and **e** marking its cell faces. Points **WW**, **W**, **P** and **E** are known and have assigned values indicated by the letter Φ. The wind flows in this example to the right, so there is one point to the right of the cell faces needed in order to calculate their value. By fitting a quadratic function through three points, both Φ_w as well as Φ_e can be determined. In the actual simulation this procedure is done in three dimensions and repeated with every iteration the simulations is run. Due to its quadratic fit, QUDS is a higher-order differencing scheme, hence making it more accurate in comparison to an upwind differencing scheme (UDS). Throughout this research simulations are preferably run using the QUDS method.

3 Results and Discussion

In this research results consist of, first of all, validating the model that calculates the LAD profile for various trees and secondly, running actual simulations using the $k-\epsilon$ turbulence model together with the theory describing transport of pollution. All calculations of LAD profiles and their subsequent discretizations were done in Matlab [Mat, 2017], while the simulations of the turbulence models were done using the HPC11 cluster at the University of Technology in Delft.

3.1 Validating LAD model

Several papers providing experimentally derived LAD profiles together with the parameters needed by the Matlab model in this research, were available and are essential to examen the model's accuracy. In appendix A-2 the code of the model is displayed. A comparison between two datasets and calculated LAD profiles concerning a pine forest, using the LAI as well as parameter L_m directly, are shown in figure 4 below:

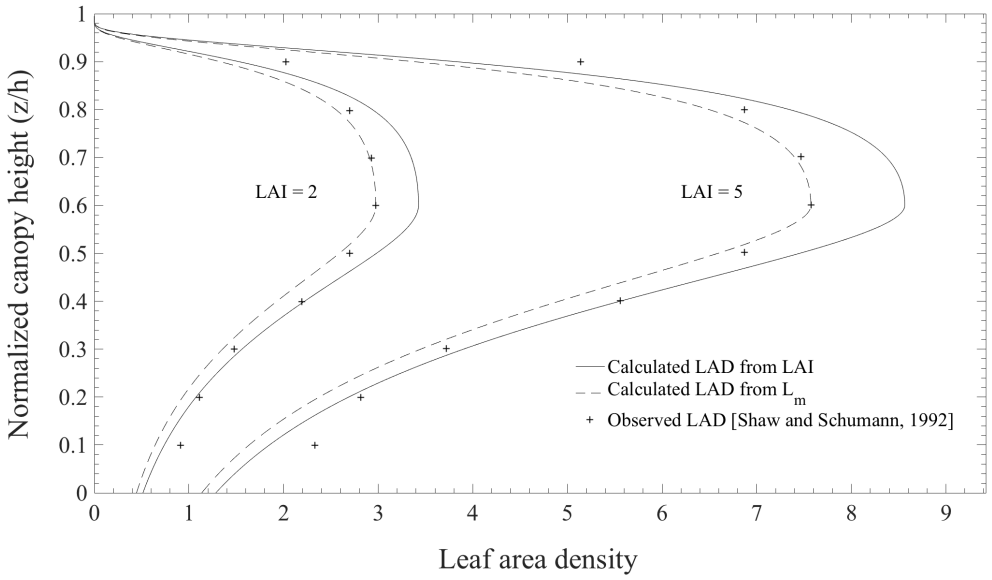

Figure 4: Calculated and observed vertical profile of the LAD for two values of LAI in a pine forest. The LAD is normalized by multiplying by the canopy height.

It appears that for calculated LAD profiles where the known value of parameter L_m is used — meaning it did not needed to be indirectly calculated according to the procedure as explained at the end of subsection 2.6 – the results show the closest resemblance to measured LAD profiles from experimental data. When first calculating parameter L_m from the LAI value, provided in the same experimental datasets, the resulting LAD profile shows higher values, hence it is shifted to the right. The contrast between computing L_m from the LAI or using it directly to calculate the LAD profile can be explained when considering the derivation of equation (2.6–2). The equation, together with the values of n applied on two different intervals, was derived using eight datasets for which all the necessary parameters, namely h, z_m and L_m, were known, as well as the actual LAD. Besides the to be deduced equation, parameter n was still unknown and is actually

derived from the datasets. For every dataset, L_m was directly substituted, instead of the calculating it indirectly from the LAI, in order to derive equation (2.6–2) as n was an unknown parameter at first; hence calculating the LAD profile in this manner shows the greatest similarities with the datasets. Calculating L_m in advance indirectly from the LAI would be dependent on used values of n, while L_m itself, as parameter with a given value, is independent of n. When using the LAI instead, equation (2.6–2) computes the parameter L_m indirectly, showing an error of not larger than 15% in comparison with L_m's actual value. Moreover, this error is the largest error found in the overall LAD profile, as L_m represents the maximum value of the LAD. The error decreases towards 0% when moving away from L_m, which is located by definition at height z_m as can be seen in figure 4.

3.2 First test case

The performance of the simulation model is first tested by comparing results with a case study, considering a Hawthorn hedge, found in: *Modelling the size-dependent collection efficiency of hedgerows for ambient aerosols* [Tiwary et al., 2006]. The experiment conducted in the case study has already been considered using the same simulation code as is used in this research [Tierolff, 2018]. Several recommendations for parameters, showing the best agreement with the experiment, as well as the general simulation specifications are replicated from the previously ran simulation.

The height of the hedge (H) is 2.2m and its width (W) is 2m. In the y-direction, the hedge has a total length of 20m. Concerning the computational domain, space before the hedge in the x-direction is 30.4m/15.2W and space after is 64m/32W. No extra space was added in the y-direction and, naturally, only space was added above the hedge in the z-direction, covering 19.8m/9H. The total domain then is 96 x 20 x 22m^3, where the maximum cell size amounts 2 x 4 x 2m^3 and at the obstacle 0.05 x 0.5 x 0.05m^3. The created mesh consists of 131 x 25 x 85 control volumes and is displayed below in figure 5 for the x-z plane:

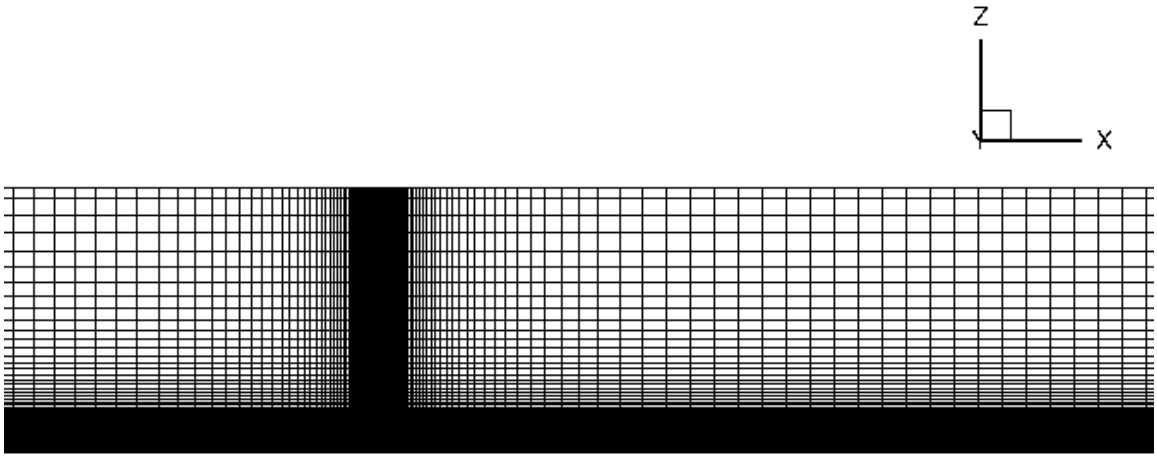

Figure 5: Created grid as used in first test case.

The LAD profile of the Hawthorn hedge was provided in the experiment and is discretized into 11 bins. It could also be calculated by the empirical model using the parameters given in the case study. Figure 6 below shows the two LAD profiles, for which simulation results can be compared, in a single plot:

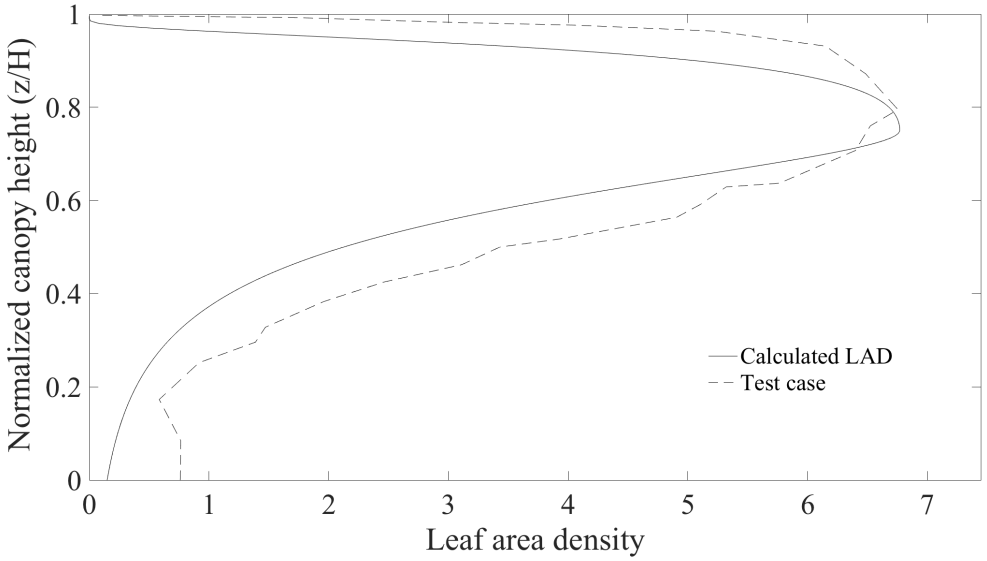

Figure 6: LAD profile from case study plotted together with calculated one.

From the LAD profile provided in the case study, parameter $L_m = 6.77$ at a height $z_m/H \simeq 0.75$ could be retrieved, so no indirect calculation using the LAI was needed. With parameter $H = 2.2$m also given, the LAD profile could be calculated using the Matlab model as the three needed parameters are known. Figure 6 shows that the calculated LAD profile is smaller by a maximum value of about 1, with the least difference at the beginning and end point of the canopy height as well as at z_m/H, where the two graphs touch. A smaller LAD profile indicates a less dense foliage and hence would suggest higher concentrations to be observed when comparing simulation results later on between the two LAD profiles. The maximum value with which the two profiles differ is highly dependent on z_m/H, which sits around 0.8. On the interval between $z/H = 0$ and $z/H = 0.2$ the LAD profile from the case study does not tend to zero but stays constant, which can be explained by the woody stem of the Hawthorn making a local increase of the LAD possible. Moreover, the LAI, which was not provided in the case study, could be reversely calculated using the Matlab model and has a value of around 2.6.

For the inlet wind velocity, the classical logarithmic profile is used, given by:

$$\frac{u}{u^*} = \frac{1}{k} \ln\left(\frac{z + z_0}{z_0}\right) \tag{3.2–1}$$

With z_0 the roughness height, reading 0.01892m, k the Kármán constant having a value of 0.41 and u^* the friction velocity, which is recommended to have a value of 0.1903m/s. The inlet profile of the wind velocity has a major influence on the overall simulation outcome and needs to be determined precisely in order to retrieve correct results.

Another important parameter is the drag coefficient, which was compared for different values with measured data from the experiment and found to show best agreement when having a value of $C_D = 0.19$ [Tierolff, 2018].

To test simulation results and compare them with the ones obtained when implementing the calculated LAD profile, several parameters are chosen from the case study. The particle diameter is set to $D_p = 15\mu$m and the leaf width of the hedge to $l = 0.005$m. The Hawthorn hedge is first assumed to be a pure broadleaf collector, meaning the deposition velocity as described in subsection 2.5, is calculated solely using the broadleaf model.

The first simulation run, is identical to the one run by Tierolff [2018] when considering the case study and the resulting concentration field is shown in his MSc thesis report in figure 14.A [Tierolff, 2018]. In the second simulation run, all parameters are kept identical and only the LAD profile provided in the case study is changed with the one calculated by the empirical model. Figure 7 below shows the results of the concentration field from the two simulations:

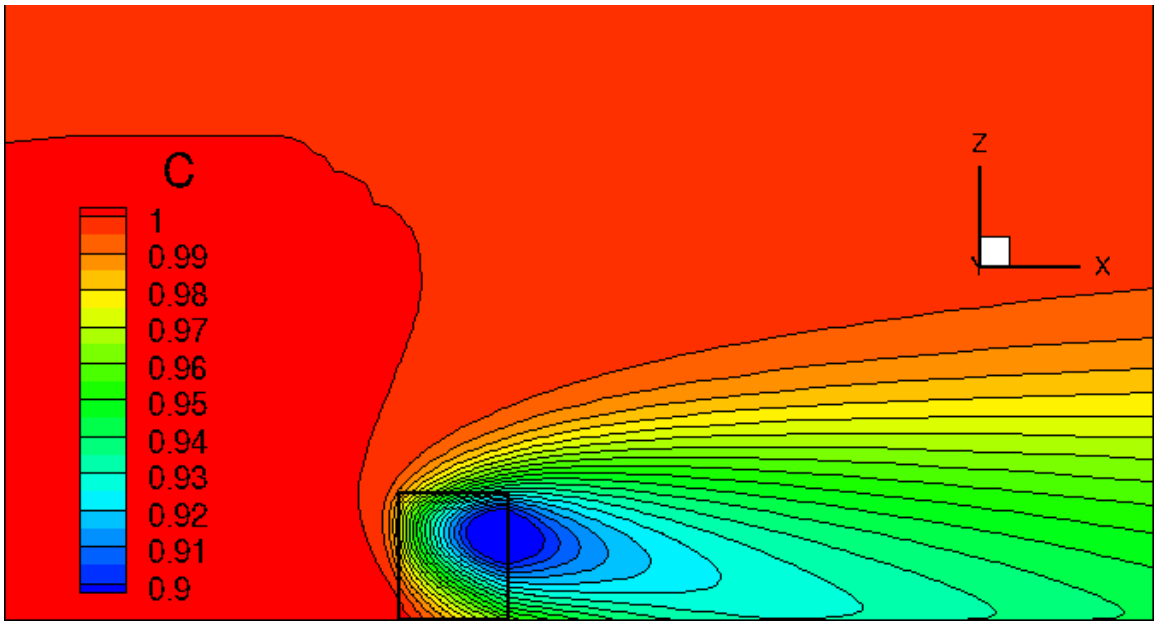

(a) Simulation with provided LAD profile.

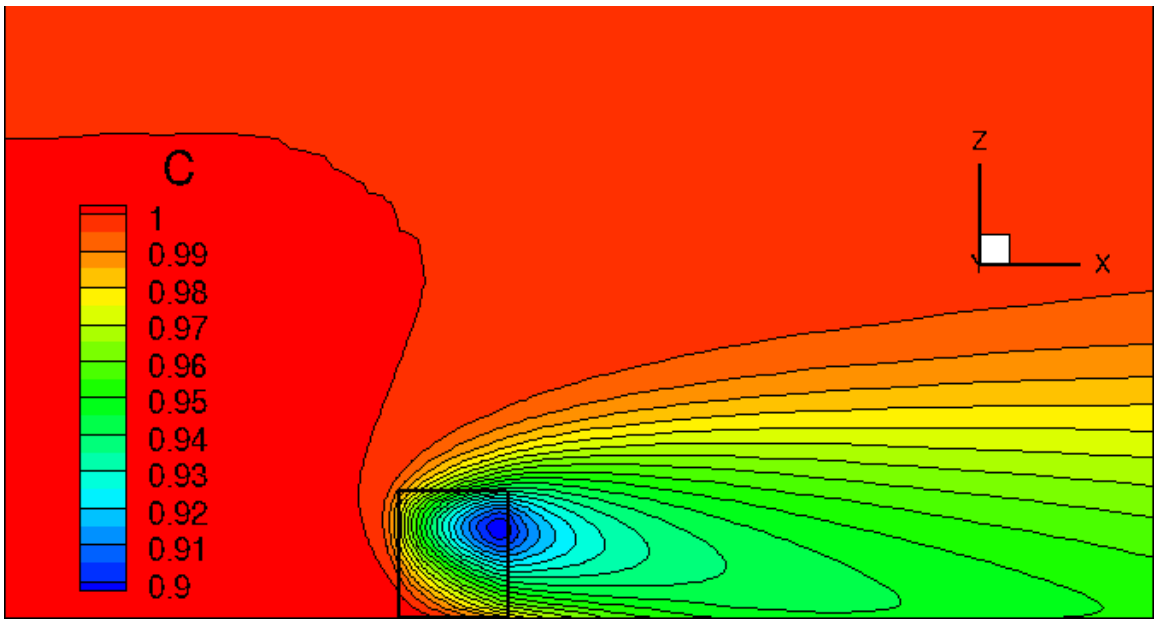

(b) Simulation with calculated LAD profile.

Figure 7: Concentration field from simulation using same specifications but two different LAD profile's.

The lowest concentration is observed at the upper half of the hedge around the downwind edge. This corresponds to the largest value of the LAD which is located at

$z_m/H = 0.75$. The fact that the lowest concentration is situated around the downwind edge makes sense as the particles have passed the longest distance inside the canopy when they arrive at this point. After the hedge the concentration increases again as lower and higher particle concentrations in the air meet and get mixed.

When looking at figure 7(a), extremely similar results are generated in comparison to those of Tierolff [2018] as expected, because identical simulation specifications were used. However, results were not exactly the same and values, especially in the region where the concentration is the lowest, differed with $0-2\%$. This small deviation can be explained by minor specification differences when running the simulation, like the scaling factor which has influence on the inlet velocity profile.

More interesting is comparing figure 7(a) to 7(b). The latter shows an overall slightly higher concentration field, but both figures hold very similar characteristics. The difference in simulated concentration field can be explained when looking back at figure 6, showing the two LAD profiles in a single plot. Because the calculated LAD profile, used to run the second simulation shown in figure 7(b), is smaller than the one provided by the case study, the canopy of the hedge is less effective in decreasing the particle concentration. This result hence agrees with the previously done prediction when discussing the difference between the two LAD profiles from figure 6.

Two velocity profiles are extracted from the simulation results at $x/H = 0.1$ and $x/H = 10$ behind the hedge. All the simulation specifications are kept unchanged and the LAD profile provided by the case study is used. In the case study, measurements of the velocity at the same position behind the hedge are performed at three heights, namely at $z/H = 0.25$, $z/H = 0.50$ and $z/H = 0.75$ [Tiwary et al., 2006]. Figure 8 below shows the simulated velocity profiles together with measurement data:

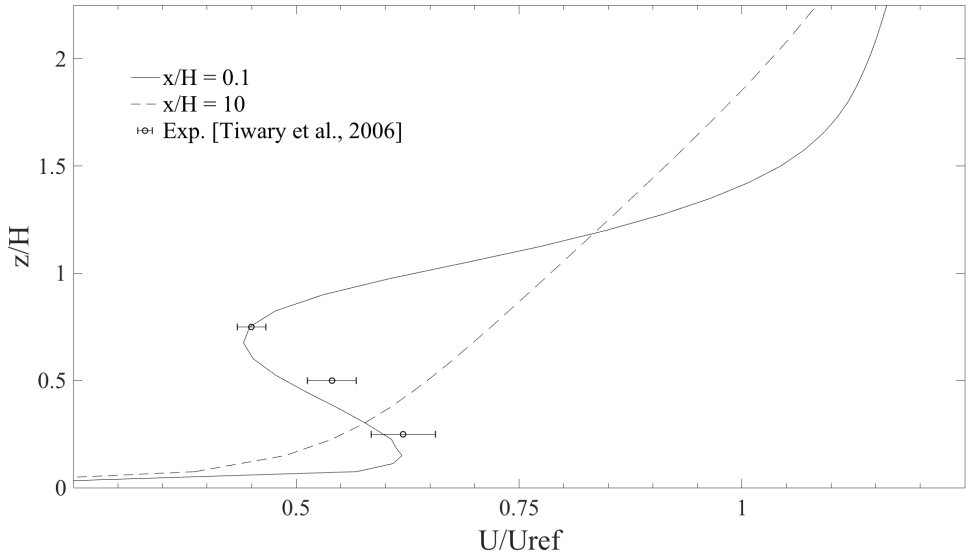

Figure 8: Velocity profiles retrieved at $x/H = 0.1$ & $x/H = 10$ together with measurement data.

Considering the velocity profile at $x/H = 0.1$, the maximum value of the LAD is located around $z/H = 0.75$ and therefore a decrease in velocity can be observed near this location. The velocity increases again after this point, reaching eventually the free stream velocity. At $z/H = 0.50$, the model underpredicts the wind velocity with respect to the measurement. The drag coefficient largely influences the velocity profile in the region $z/H = 0.40 - 0.75$ and when using a slightly lower drag coefficient, like $C_D = 0.17$, better

matching results could be achieved with this measurement point. However, the wind velocity would then again be overpredicted at $z/H = 0.75$, where the drag coefficient has the most impact. Velocity profiles that are extracted farther behind the hedge do not show the characteristic increase to decrease to, again, increase, because the wind velocity at this point is already distributed more evenly. Instead, they show a solely increasing wind velocity with increase in height. An example is shown by the velocity profile retrieved at $x/H = 10$, marked with the dashed line in figure 8.

In validating the performance of the simulation model, a final comparison is done considering the collection efficiency for different particle sizes. The collection efficiency (CE) is defined as:

$$\text{CE} = \frac{C_{in} - C_{out}}{C_{in}} \tag{3.2–2}$$

with C_{in} and C_{out} the particle concentration measured at $x/H = 0.1$ upwind and downwind respectively at a height $z/H = 0.75$. Specifications of the simulation are adopted to the recommended ones in order to achieve best matching results with the experimental data. The hawthorn hedge is not considered a solely broadleaf collector anymore, but instead a combination of a broadleaf and needle-like collector. Leaf hairs and thorns of the hedge namely increase the deposition velocity and hence the hedge should be represented as partially a needle-like collector. Using a distribution variable ϕ, the respective weight between the two types of collectors, each with their corresponding deposition velocity model, could be set with the following relationship: $\bar{U}_k(d_p) = (1-\phi)\bar{U}_k^{broad} + \phi\bar{U}_k^{needle}$ [Šíp and Beneš, 2016]. The mean leaf width is provided in the case study and is set to $l = 0.022$m, whereas the needle diameter is estimated to $d_N = 0.0005$m. The distribution variable is recommended to have a value of $\phi = 0.30$ [Tierolff, 2018]. Multiple simulations are run, using identical particle diameters as were measured during the experiment. Figure 9 shows the results of the CE:

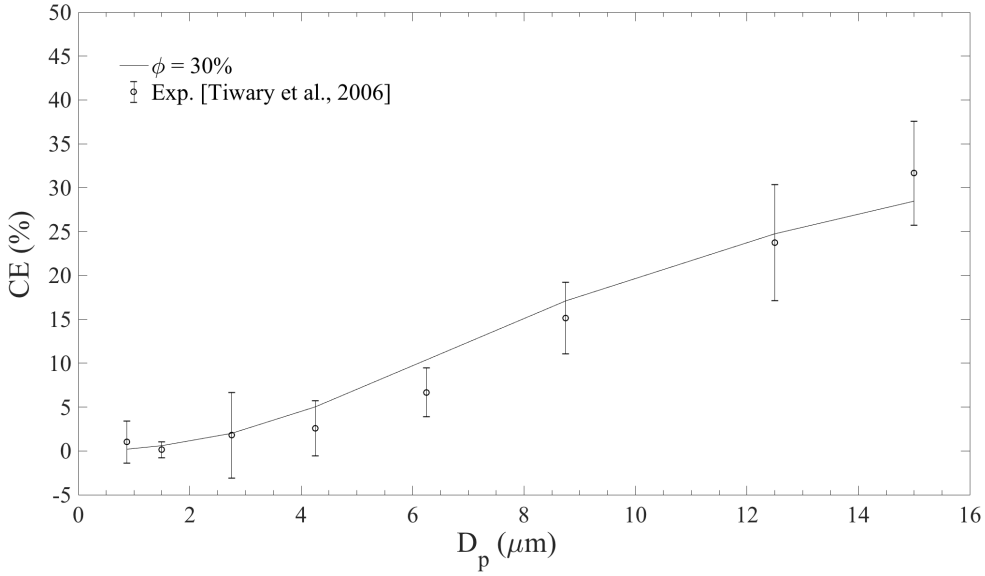

Figure 9: Simulated concentration efficiency together with measurement data.

Simulation results clearly show the trend of increasing CE for particles of larger size. The results match the experimental data well, except for $D_p = 6.25\mu$m, where the model overpredicts the CE. By lowering ϕ, the CE will be lowered as the proportion of fine needle-like collectors, with corresponding higher deposition velocities, is decreased. However,

CE results at other measurement points, including at $D_p = 15\mu m$, will all be lowered simultaneously.

3.3 Second test case

After initially testing the performance of the RANS simulation model, results of a second case study obtained with large eddy simulation (LES) turbulence model are compared; the results are found in: *Roadside vegetation barrier designs to mitigate near-road air pollution impacts* [Tong et al., 2016]. The more complicated LES model was initially evaluated against the same dataset [Hagler et al., 2012] adapted by a previous research [Steffens et al., 2012], which used the comprehensive turbulent aerosol dynamics and gas chemistry (CTAG) model in addition to RANS to simulate vegetation effects on polluting particles. Although discrepancies were present, results from LES compared to the original dataset showed overall close agreement [Tong et al., 2016].

Common near-road configurations are drafted, consisting of only vegetation or a combination of vegetation and a physical barrier. The vegetation is represented by a mixture of coniferous evergreens, like Pine and Cedar, meaning only the needle-like velocity deposition model is used. The needle diameter is estimated to $d_N = 0.005$m based on these tree species. The case study uses the same LAD profile as the one provided by Steffens et al., [2012]. It was claimed to be calculated as described in subsection 2.6, using equations (2.6–2) and (2.6–3). Subsequently, two LAD profiles are calculated having similar parameters: one using the unadjusted theory to compare results, the other using adjusted intervals for n in equation (2.6–1) in order to reproduce the provided LAD profile. Figure 10 shows the three LAD profiles in a single plot:

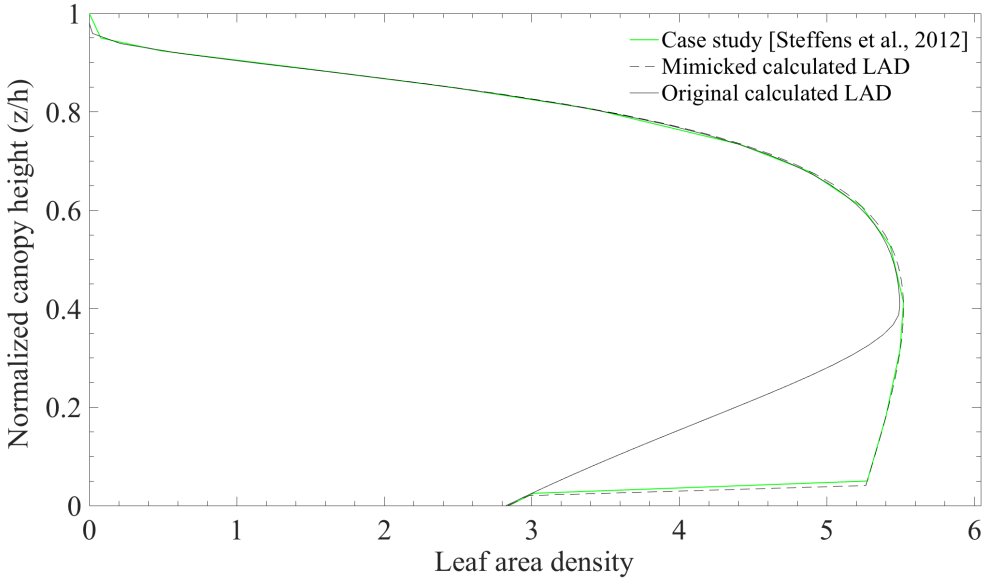

Figure 10: LAD profile used by case study plotted together with calculated ones.

The provided LAD profile shows a distinctive nod around $z = 0.04h$, which indicates equation (2.6–1) was adjusted by modifying the lower interval from $0 \leq z < z_m$ to a relatively small region $0 \leq z < 0.04h$, still having the same value $n = 6$. Furthermore, the upper interval of n, going from $z_m \leq z \leq h$, is modified to occupy the remaining region

$0.04h \leq z < z =\leq h$. In summary, the original equation (2.6–1) for n is changed to:

$$n = \begin{cases} 6, & 0 \leq z < 0.04h \\ \frac{1}{2}, & 0.04h \leq z \leq h \end{cases} \tag{3.3–1}$$

It is striking that the new boundary of the two intervals is not anymore where it should be, namely at $z_m(= 0.4h)$, but instead at $z_m/10(= 0.04h)$. Possibly a mistake was made, as the calculated LAD profile with modified intervals of n appears unnatural in comparison to the calculated LAD with original intervals of n. The LAI is measured with a LAI-2000 plant canopy analyzer and has a value of LAI $= 3.3 \pm 1.0$ [Hagler et al., 2012]; when constructing the original LAD from figure 10, the LAI is actually set to LAI $= 4$. The provided LAD profile is divided in 14 bins and used later on.

The computational domain has dimensions 227 x 150 x 50m^3 and is divided in 248 x 70 x 160 control volumes. The maximum cell size is 2 x 4 x 2m^3 and at the obstacle 0.1 x 1 x 0.05m^3. A logarithmic inlet velocity profile normal to the barrier is generated using formula (3.2–1), with an average inlet velocity of $u = 2$m/s [Tong et al., 2016]. The roughness height has a value $z_0 = 0.6$m, appertaining to the given coniferous canopy [Katul et al., 2004], whereas the friction velocity reads $u^* = 0.382$m/s. The particles in the case study have diameters D_p ranging from 15nm – 253nm, with density $\rho_p = 1500$kg/m^3 [Hagler et al., 2012]. Moreover, they experience a plant drag coefficient, having a value of $C_D = 0.2$ [Katul et al., 2004]. Important to note is that the particles are not anymore released from the domain inlet, but from a highway emission zone reaching 0.5 to 2 meters in height, with a width of 12m.

The baseline configuration considers a row of 6m tall trees, 12m wide, located at 3m away from the road. Figure 11 gives a schematic representation of this configuration, including appropriate proportions:

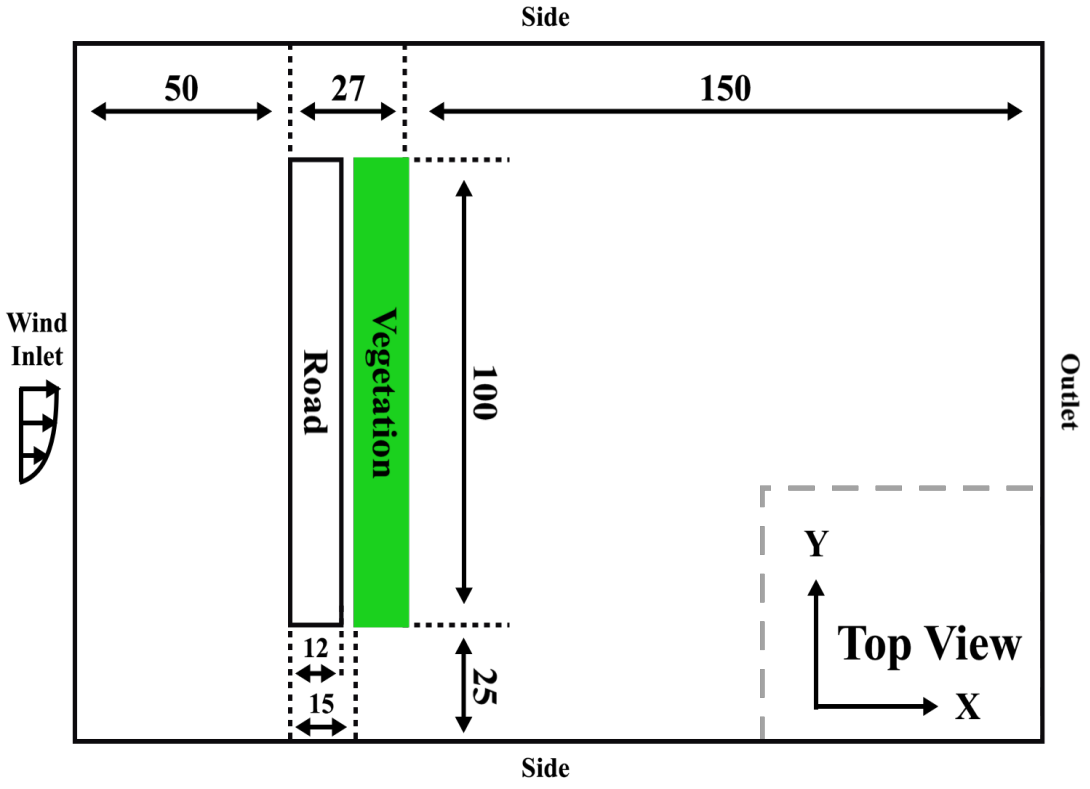

Figure 11: Schematic representation of baseline configuration.

Furthermore, figure 12 shows the created mesh for the x-z plane:

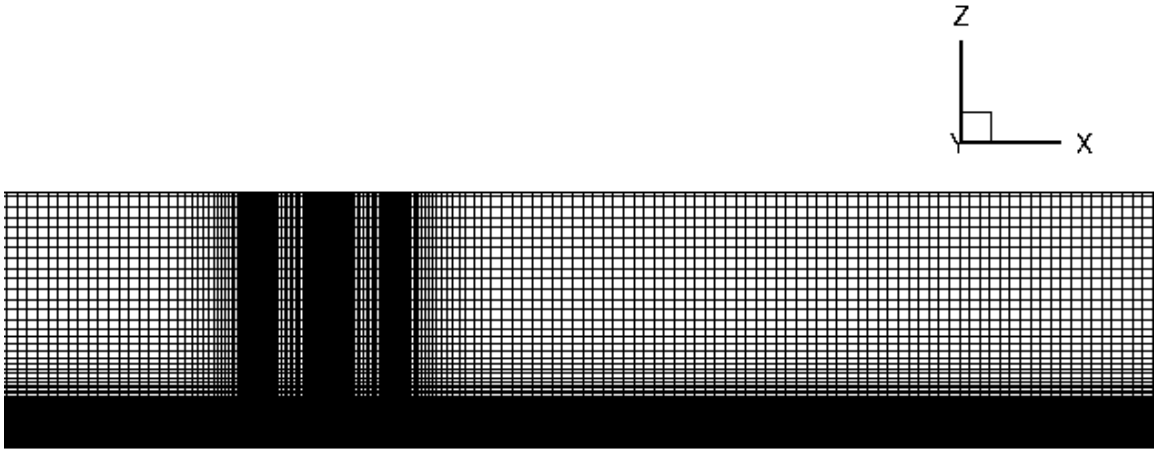

Figure 12: Created grid as used in second test case.

At the location of the highway emission zone a finer mesh is chosen, in order to accurately track the concentration of the particles. The first vertical dense grid lines visible, represent the start of the road, whereas the second indicate the end of the road together with the start of the vegetation 3m behind it. The third and last vertical dense grid lines indicate the end of the vegetation.

To start off, instead of emitting the particles from the highway emission zone, they are released from the inlet, identical to the first test case. Doing so enables to create a first impression of the new setting, consisting of a different domain, velocity profile, LAD profile and so on. Figure 13 shows the resulting concentration field from such simulation using $D_p = 100$nm:

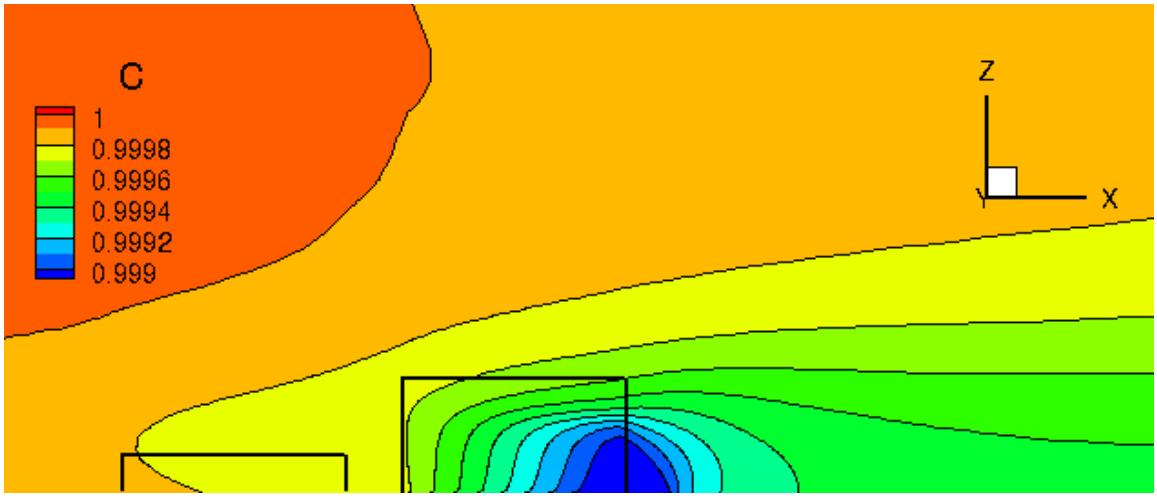

Figure 13: Concentration field using model from first test case, $D_p = 100$nm.

The results are as expected; because the entire domain has a particle concentration of one as initial condition, the concentration field shows relatively high values. The first square indicates the 2m tall highway emission zone, deactivated during this simulation, and the second square the 6m tall vegetation. The lowest concentration is witnessed around the downwind edge of the tree stands, just like in the first test case. The fact that the canopy does not reduce the concentration with roughly 10% like then, but with

merely 0.1%, can be explained because of the small particle diameter now used. The canopy is much less effective in reducing particle concentration for these smaller sized particles, implying their deposition velocity is lowered significantly.

The model is slightly adjusted so that the particles will be released solely from the highway emission zone. The particle concentration normalized by the peak concentration from a no-barrier case at corresponding particle size is measured and defined by the letter χ. The concentration field of the no-barrier case is shown in figure 14 and in order to compare results, the concentration field of the baseline configuration using $D_p = 15$nm is shown in figure 15:

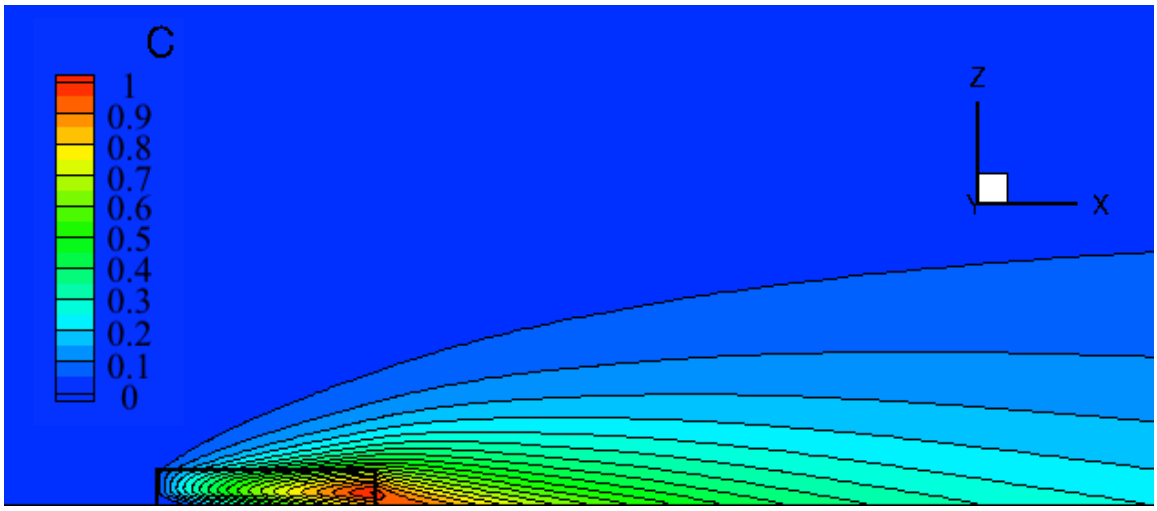

Figure 14: Concentration field no-barrier case, $D_p = 15$nm.

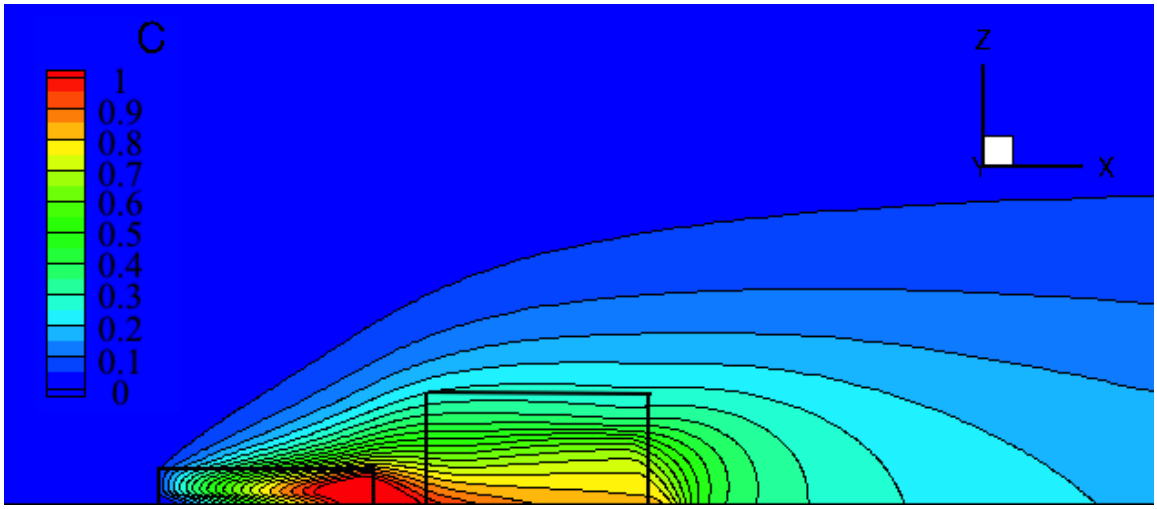

Figure 15: Concentration field baseline configuration, $D_p = 15$nm.

In contrast to figure 13, which shows the concentration field generated using the model from the first test case, the concentration is overall low in both plots. The highest concentration can be observed at the end inside of the highway emission zone, as the particles are released from the entire zone and pushed due to perpendicular wind to the end of the road, where subsequently accumulation of the particles takes place. The particles in the no-barrier case just undergo dispersion with no vegetation barrier present, which is well noticeable by the scattering of particles behind the emission zone.

Results differ, logically, regarding the baseline configuration. Due to the particles decelerating upwind to the vegetation barrier in addition to their accumulation at the end of the road, the on-road concentration is elevated in comparison to the no-barrier case. In between the highway emission zone and the vegetation barrier, similar patterns of scattering due to dispersion can be observed as in the no-barrier case. Within the vegetation, the concentration remains about constant after it decreases instantly, immediately behind the barrier. A sharp drop in concentration makes sense as the particles with $D_p = 15$nm are the smallest particles to be tested and hence should show a higher deposition velocity than larger particles would. The fact that the sharp drop occurs behind the vegetation barrier instead of within is not expected and needs to be investigated further using the normalized concentration results for different particle sizes.

In order to obtain correct normalized concentration results, the location of the peak concentration in the no-barrier cases needs to be determined first using figure 14, plotted using $D_p = 15$nm. Its location is in the on-road regime, at 11.85m distance and 0.70m height. Like in the case study, all the data measurements are performed over a distance of 100m, starting from the road. The measurements are performed at the corresponding height of the peak concentration of the no-barrier case to ensure valid results; that is in general at $z = 0.70$m. Figure 16 includes measurement data from the case study as well as the most essential results generated, after performing multiple simulations:

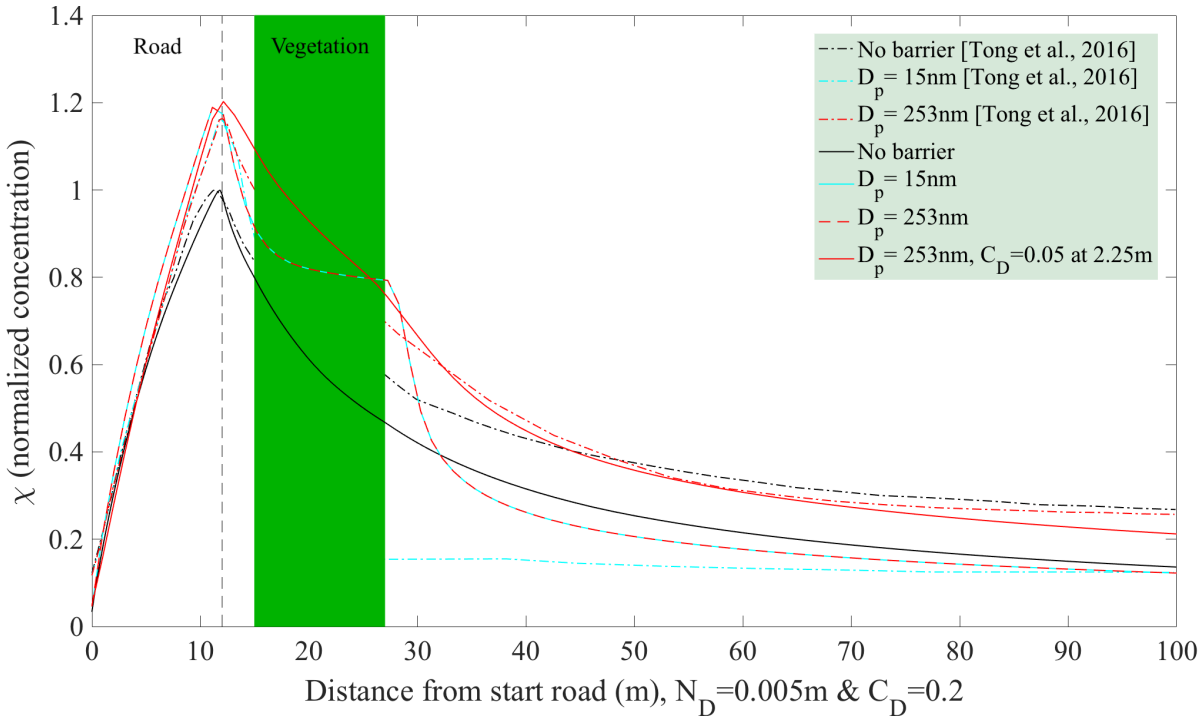

Figure 16: Normalized concentration profiles together with provided data.

Concerning the different particle sizes tested in the case study, only concentration profiles of the smallest and the largest ones, respectively 15nm and 253nm in diameter, are plotted. The simulation results for these and all other particle sizes in between are identical, which strongly disagrees with the results provided by the case study. The discussed constancy of the particle concentration from figure 15 within the barrier as well as the sharp drop behind it, are again well visible in figure 16 and evidently apply also to the plotted particles with $D_p = 253$nm.

When comparing the simulated results of $D_p = 15/253$nm with those from the case study, both have similar concentrations profiles in the on-road regime. They reach a normalized concentration value of around 1.2, which is an increase of roughly 20% with respect to the no-barrier case. Same argument can be made as was given for the results in figure 15 in the on-road regime: the on-road particle accumulation upwind to the vegetation barrier together with the deceleration of the perpendicular moving wind, causes the local increase in particle concentration.

The simulated concentration profiles of $D_p = 15/253$nm inside the vegetation are highly unrealistic and differ strongly with those provided by the case study. The concentration remains almost constant within the vegetation, after it sharply drops behind the barrier. Based on multiple simulations run, needle diameter, particle density and reference velocity do not explain this result; nor does the particle diameter – figure 18 shows that a result with similar characteristic is already obtained using $D_p = 5\mu$m. Furthermore, the velocity profile, as always, has large effect on simulation results, but varying this would change concentration profile results not only for the barrier regime, but the entire domain. Measuring concentration profiles at different heights, like at 2m, 3m or even 6m, only makes results worse. However, one parameter that majorly influences the results for particles with diameters in the nanometer range, is the plant drag coefficient C_D. With an unrealistically low value of $C_D = 0.05$ and a measuring height of 2.25m – for a drag coefficient this low, changing the measuring height in contrast does improve the normalized concentration results with respect to the case study – best agreement could be achieved with the results of $D_p = 253$nm. When continuing the trend of decreasing C_D, one quickly arrives at $C_D = 0$ which represents the no-barrier case in this study; in this case, the vegetation does not interact with the particles whatsoever according to the theory described in subsection 2.4.

Looking at the no-barrier case, results of the simulation and the case study are quite similar. From the start of the vegetation barrier until the end of the domain, the simulated plot decreases faster and eventually reaches $\chi \approx 0.1$. In the y-direction, there is an empty space of 25m created at each side of the domain. When this empty space is neglected, the two plots better agree, as the particles from the simulated case cannot disperse to the sides of the domain anymore, resulting in a higher normalized concentration profile.

The dry deposition model, constituted in Tierolff [2018], suggests to not realistically predict particle movement of the particle sizes tested in the case study. From all different factors influencing the deposition velocity as discussed in subsection 2.5, the only deposition process that has increasing effect with decreasing particle diameter is Brownian diffusion [Petroff et al., 2008]. Figure 5.A in Tierolff [2018] as well as figure 1.A in Šíp and Beneš [2016] support this claim, showing a major shift from several different deposition processes acting in the micrometer range to Brownian diffusion gaining dominance in the nanometer range. However, these figures also suggest interception still may play an active roll for particles with $D_p > 100$nm, or perhaps even lower.

To test if this argumentation indeed explains the obtained results, the dry deposition model is turned completely off, while the plant drag coefficient is kept unchanged at $C_D = 0.2$. Results are shown in figure 17:

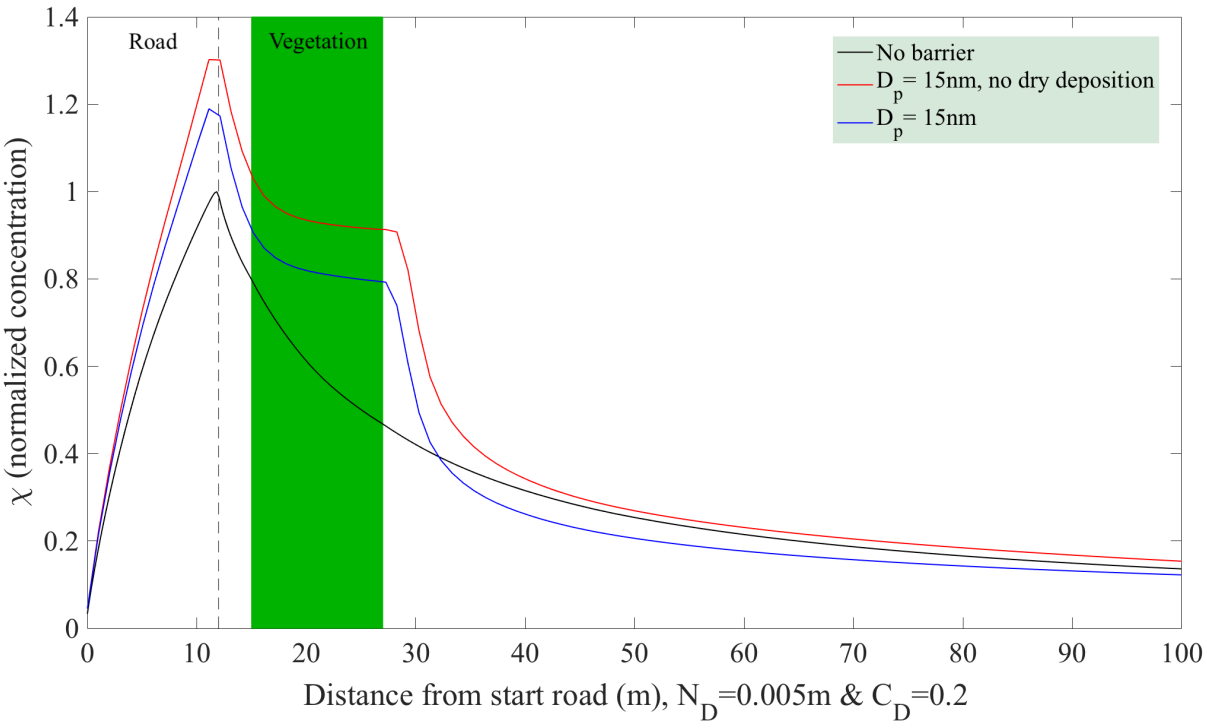

Figure 17: Normalized concentration profiles together with dry deposition model turned off.

The results apodictically falsify the previous proposed reasoning, as the only difference between having the dry deposition model active or not, is the fact that the overall concentration with the latter is higher due to the various deposition processes not acting on the particles anymore. With no dry deposition, the unexpected sharp drop behind the vegetation barrier is still visible, while the concentration remains almost constant within the canopy. On the other hand, the strong dependency between the concentration profile and the plant drag coefficient, together with the theory provided in subsection 2.4, give rise to a renewed argumentation: regarding this specific study, the current $k-\epsilon$ turbulence model does not realistically predict particle movement of the concerning particle sizes. The interaction between nano-sized particles and the vegetation barrier cannot correctly be modelled. In the no-barrier case, the dry deposition model is still active, strengthening this argumentation only more as the concentration profile shows a natural decline within the vegetation similar to the results provided by the case study.

The simulated results show that the vegetation with $C_D = 0.2$ is retaining the small sized particles, resulting in a constant concentration profile, while almost no dispersion takes place. The sharp drop behind the vegetation can simply be explained by a mass balance analysis. While the normalized concentration of particles remains constant around $\chi = 0.8$ within the canopy, there are no particles left to provide for a realistic decline in concentration behind the barrier. Instead, it appears hyper dispersion has taken place, eventhough this is not the case. Eventually, the particle concentration approaches the plot of $D_p = 15$nm from the case study around 25m downwind of the barrier. In appendix A-1, a brief summary of the reasoning behind the expected results from the case study is given.

In the first test case, the performance of the simulation model was tested using particles with diameters in the micrometer range. Three different particle sizes in this range are plotted in figure 18:

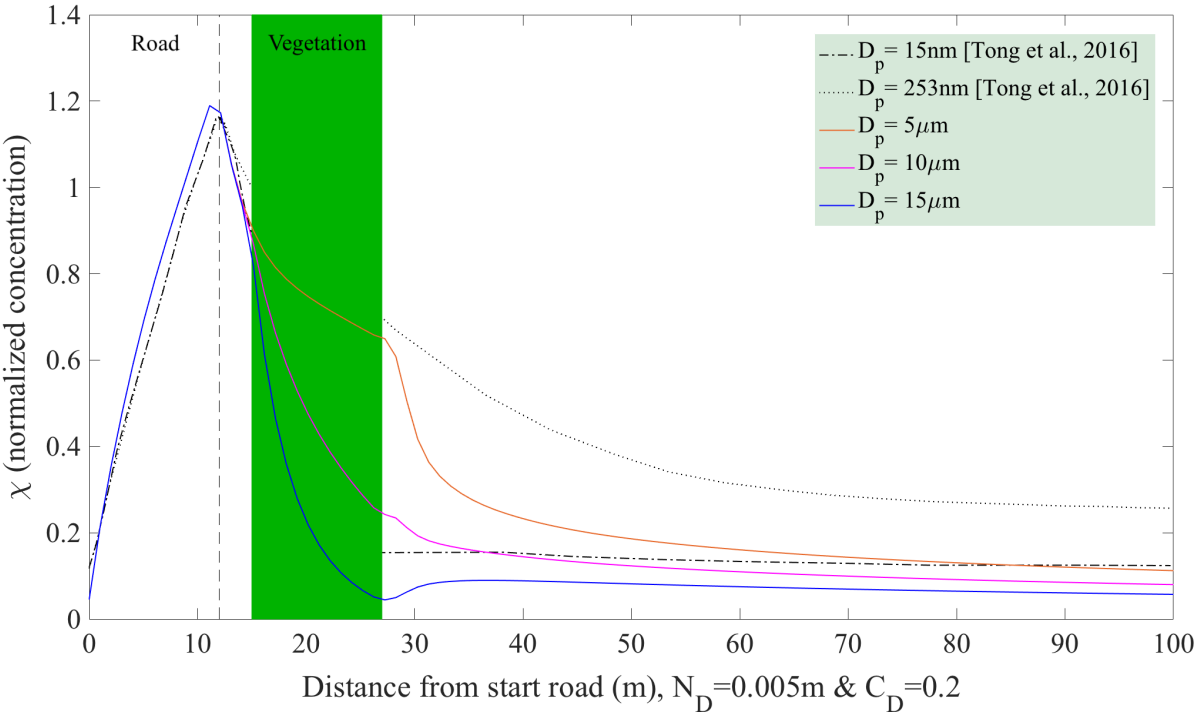

Figure 18: Normalized concentration profiles in µm-range together with provided data.

All three show a much more natural deposition process within the vegetation barrier, followed by a small decline due to dispersion. Particles with $D_p = 5\mu$m already start to approach a similar concentration profile as those of the $D_p = 15/253$nm plots. These three plots indicate that current turbulence model does not lack to produce realistic simulation results for larger particle sizes.

The turbulent kinetic energy and velocity fields are plotted in figures 19 and 20:

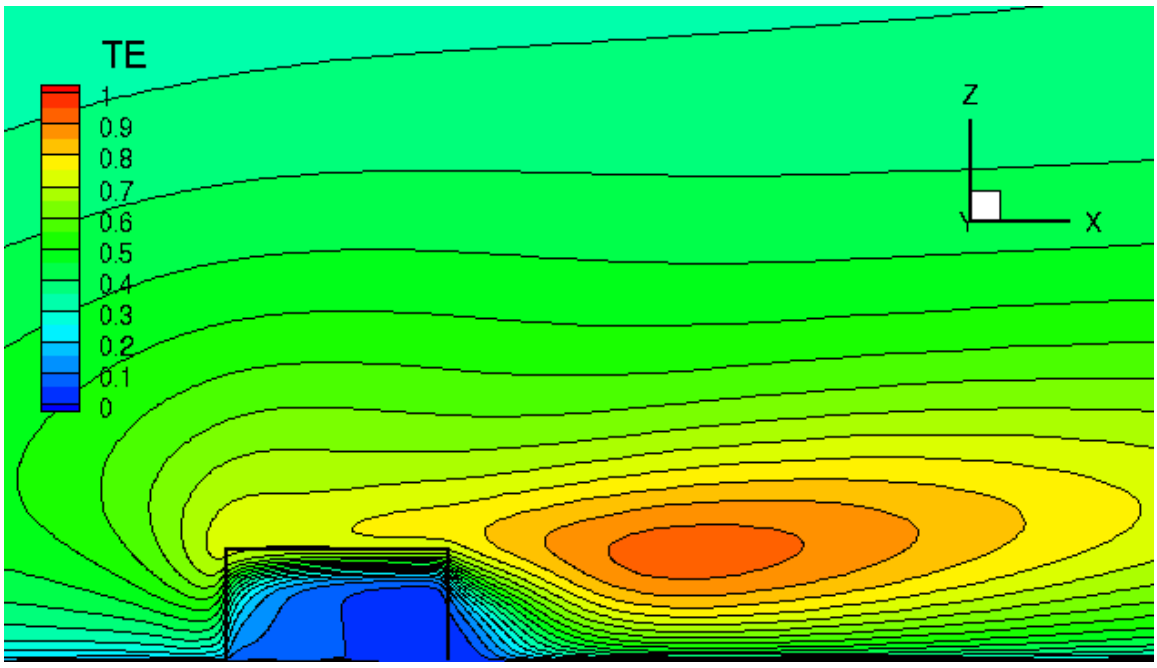

Figure 19: TKE field, baseline configuration with $D_p = 15$nm.

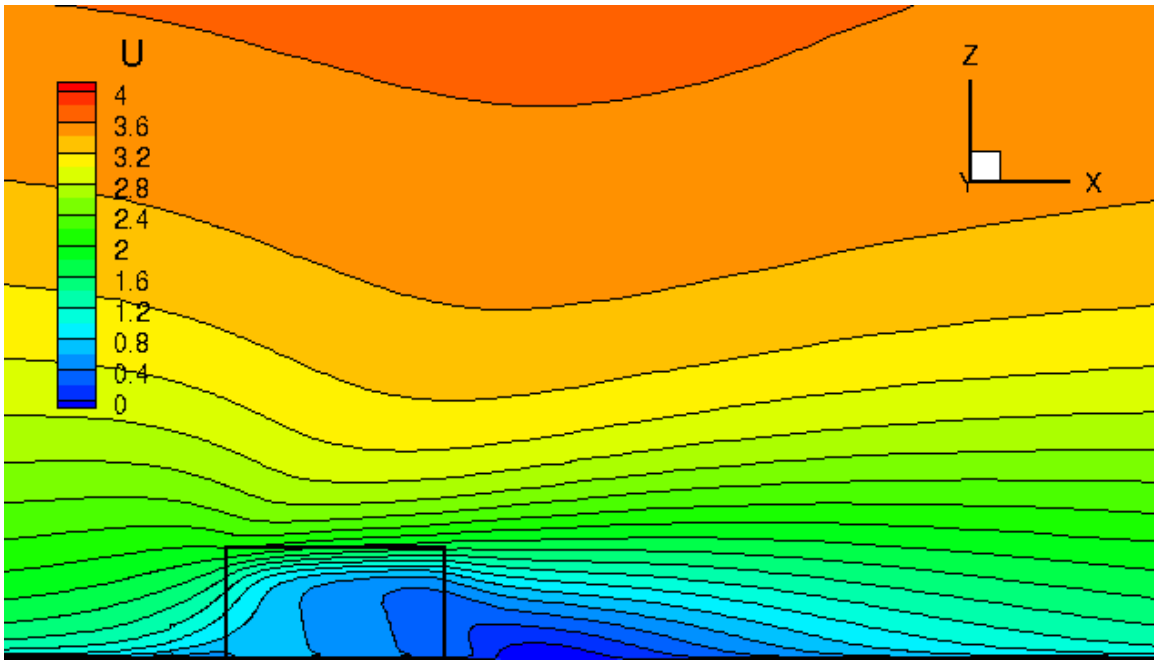

Figure 20: Velocity field, baseline configuration with $D_p = 15$nm.

Inside vegetation barriers, especially forest canopies, there usually forms a sink of TKE when the LAD or plant drag coefficient increases, as leaves act as turbulence suppressors [Kenjereš and Ter Kuile, 2013]. Referring back to subsection 2.4, leaves inside the canopy namely generate small-scaled eddies causing a quick dissipation of TKE. Moreover, larger generated eddies behind the obstacle due to shear causes acts as a source of TKE. Both processes are well visible in figure 19, showing a region of low TKE within the vegetation barrier, followed by a region of high TKE just behind it. Another interesting aspect is the fact that both the high region of TKE in figure 19 and the hyper dispersion of particles visible in the same region, looking back at figure 15, confirm each other; higher TKE means an increase in turbulent mixing, leading to a faster dispersion of particles [Šíp and Beneš, 2016].

The velocity within the canopy decreases substantially due to the drag imposed by the vegetation, as is shown in figure 20. However, it reaches its lowest value behind the canopy, where a strong velocity gradient is created. When looking upwind to the vegetation barrier, part of the logarithmic inlet velocity profile can be recognized.

4 Conclusion

In this research, an empirically derived leaf area density (LAD) model is implemented in Matlab and used to calculate and discretize LAD profiles of various tree and plant species. In the model, crucial parameter L_m, representing the maximum value of the LAD, can be obtained by numerically integrating the LAD function in the case its value is unknown. Calculated LAD profiles using numerically obtained values of L_m are similar, although 15% too large at most, in comparison to measured LAD profiles from experimental data. As a consequence, they are slightly shifted, while closest resemblance to experimental data is obtained when using known values of L_m.

Moreover, the performance of the simulation model is tested. The results from the simulations, considering a Hawthorn hedge and particles with diameters in the micrometer range, show overall close agreement with the experimental data from the first case study provided by Tiwary et al., [2006], as well as with the previously obtained results from Tierolff, [2008], which uses the same simulation code as is used in this research.

Review concerning main objective study:
The simulation model is compared with a large eddy simulation (LES) turbulence model from the second case study provided by Tong et al., [2016]. A common near-road baseline configuration is drafted, consisting of a 12m wide vegetation barrier with 6m tall coniferous trees. From a highway emission zone, located upwind to the barrier, the pollutants are released. The LAD profile provided by the case study, is calculated using a slightly adjusted formula than the one used in this research and therefore shows a distinctive nod around $z/h = 0.04$. Normalized concentration results are compared and evaluated against those obtained by Tong et al., [2016], which examines particles with diameters ranging from 15nm – 253nm:

- An unexpected sharp drop behind the vegetation barrier is visible, while the concentration remains almost constant within the canopy; a mass balance analysis confirms this. On top of that, concentration profiles using $D_p = 15-253$nm are identical. Because the dry deposition model does not influence these observations but the plant drag coefficient drastically does, it can be argued that, regarding this specific study, the current $k-\epsilon$ turbulence model does not realistically predict particle movement of the concerning particle sizes. It is recommended to re-examine part of the theory behind the model that depends on the plant drag coefficient and describes the interaction between vegetation and fluid flow.

- The no-barrier case, with $C_D = 0$ but LAD still active, as well as a barrier case using an unrealistically low value of the plant drag coefficient, provide similar results to those found in the case study, giving rise to the same, drawn argumentation. In a future study, it is suggested to make the LAD inactive when simulating the no-barrier case, as the dry deposition model may otherwise still effect concentration results.

- Particles with diameters of $D_p > 5\mu$m, do not experience similar behavior as the nano-sized particles do, implying the turbulence model provides realistic results for larger sized particles. This corresponds with the accurate results obtained in the first test case, using particles with diameters in the micrometer range.

Variations between the most dominant deposition processes acting on particles in the nanometer range – these are presumably Brownian diffusion and perhaps also interception – could not be explored in detail with the current results. When improved results are realized, it is hence suggested to investigate the dependency of the deposition velocity on the particle diameter using identical simulation specifications to clarify the regimes in which a specific deposition process dominates relative to others. In addition, different deposition models could, moreover, be compared with one another.

At a later stage, after more realistic results are obtained using nano-sized particles, it would be interesting to perform simulations with barrier specifications varying from the baseline configuration to test the model's diversity and to be able to imitate desirable real-life barrier configurations, yielding relevant results.

References

R. Byron Bird, Warren E. Stewart, and Edwin N. Lightfoot. *Transport Phenomena*. John Wiley & Sons, Inc., New York, second edition, 1962.

P. Bradshaw, T. Cebeci, and J.H. Whitelaw. *Engineering Calculation Methods for Turbulent Flow*. Academic Press Inc. Ltd, Londen, 1981.

G.S.W. Hagler, M.Y. Lin, A. Khlystov, R.W. Baldauf, V. Isakov, J. Faircloth, and L.E. Jackson. Field investigation of roadside vegetative and structural barrier impact on near-road ultrafine particle concentrations under a variety of wind conditions. *Science of The Total Environment*, 419:7 – 15, 2012. ISSN 0048-9697. URL `http://www.sciencedirect.com/science/article/pii/S0048969711014070`.

K. Hanjalić, S. Kenjereš, M.J. Tummers, and H.J.J. Jonker. *Analysis and Modelling of Physical Transport Phenomena*. VSSD, Delft, second edition, 2009.

J.O. Hinze. *Turbulence - An Introduction to Its Mechanism and Theory*. McGraw-Hill Book Company, Inc., Londen, 1959.

G.G. Katul, L. Mahrt, D. Poggi, and C. Sanz. One-and two-equation models for canopy turbulence. *Boundary-Layer Meteorology*, 113(1):81 – 109, 2004. URL `https://link.springer.com/content/pdf/10.1023/B:BOUN.0000037333.48760.e5.pdf`.

S. Kenjereš and B. Ter Kuile. Modelling and simulations of turbulent flows in urban areas with vegetation. *Journal of Wind Engineering and Industrial Aerodynamics*, 123:43 – 55, 2013. ISSN 0167-6105. URL `http://www.sciencedirect.com/science/article/pii/S0167610513001955`.

B. Kolic. Forest ecoclimatology (in Serbian). 1978. 295 pp.

B. Lalic and D.T. Mihailovic. An empirical relation describing leaf-area density inside the forest for environmental modeling. *Journal of Applied Meteorology*, 43:641 – 645, 2004.

B.E. Launder and B.I. Sharma. Application of the energy-dissipation model of turbulence to the calculation of flow near a spinning disc. *Letters in heat and mass transfer*, 1(2):131 – 138, 1974. URL `https://ac.els-cdn.com/0094454874901507/1-s2.0-0094454874901507-main.pdf?_tid=2df5745c-0194-49e8-92a2-acc5eef372dd&acdnat=1529328424_7af15ce50326adc195b85c48de86709c`.

MATLAB version 9.2.0.556344 (R2017a). The Mathworks, Inc., Natick, Massachusetts, 2017.

A. Petroff, A. Mailliat, M. Amielh, and F. Anselmet. Aerosol dry deposition on vegetative canopies. part ii: A new modelling approach and applications. *Atmospheric Environment*, 42(16):3654 – 3683, 2008. ISSN 1352-2310. URL `https://www.sciencedirect.com/science/article/pii/S1352231008000022`.

R.H. Shaw and U. Schumann. Large-eddy simulation of turbulent flow above and within a forest. *Boundary-Layer meteorology*, 61:47 – 64, 1992.

V. Šíp and L. Beneš. Rans solver for microscale pollution dispersion problems in areas with vegetation: Development and validation. *arXiv:1609.03427*, 2016. URL https://arxiv.org/pdf/1609.03427.pdf.

J.T. Steffens, Y.J. Wang, and K.M. Zhang. Exploration of effects of a vegetation barrier on particle size distributions in a near-road environment. *Atmospheric Environment*, 50:120 – 128, 2012. ISSN 1352-2310. URL http://www.sciencedirect.com/science/article/pii/S1352231011013410.

L. Tan. Numerical comparison of models for vegetation effects on airflows using the $k-\epsilon$ turbulence model. Bachelor's thesis, Technical University Delft, July 2009.

E. Tierolff. Extending a rans solver with heat and pollution modules for dispersion problems in urban areas with vegetation. Master's thesis, Technical University Delft, May 2018.

A. Tiwary, H.P. Morvan, and J.J. Colls. Modelling the size-dependent collection efficiency of hedgerows for ambient aerosols. *Journal of Aerosol Science*, 37(8):990 – 1015, 2006. ISSN 0021-8502. URL http://www.sciencedirect.com/science/article/pii/S0021850205001515.

Z. Tong, R.W. Baldauf, V. Isakov, P. Deshmukh, and K.M. Zhang. Roadside vegetation barrier designs to mitigate near-road air pollution impacts. *Science of The Total Environment*, 541:920 – 927, 2016. ISSN 0048-9697. URL http://www.sciencedirect.com/science/article/pii/S0048969715307270.

J. Vidal. Air pollution rising at an 'alarming rate' in world's cities. 2016. URL https://www.theguardian.com/environment/2016/may/12/air-pollution-rising-at-an-alarming-rate-in-worlds-cities.

WHO. Ambient air pollution: A global assessment of exposure and burden of disease. 2016. URL http://apps.who.int/iris/bitstream/handle/10665/250141/9789241511353-eng.pdf?sequence=1.

WHO. Ambient (outdoor) air quality and health. 2018. URL http://www.who.int/en/news-room/fact-sheets/detail/ambient-(outdoor)-air-quality-and-health.

Appendix

A-1

A brief summary of the reasoning behind the results from the case study which were expected is given below for $D_p = 253$nm and $D_p = 15$nm [Tong et al., 2016]:

- Concerning the particles with size $D_p = 253$nm, it was expected their concentration profile would be greater in the immediate vicinity behind the barrier than the no-barrier case, due to reduced dispersion within the vegetation as well as the generated behind-barrier wake zone, as the general acting dispersion of particles in the no-barrier case is more efficient than the deposition of those particles due to vegetation. Roughly 20m downwind of the barrier, the concentration is lower than that of the no-barrier case, which can be explained by a mass balance.
- The particles with size $D_p = 15$nm experience a sharp drop in concentration within the vegetation barrier due to their higher deposition velocity. The concentration already is lower in around the start of the barrier than the no-barrier case. Downwind of the barrier, dispersion shows almost no effect because of the low particle concentration.

A-2

Matlab model used to calculate LAD and print obstacles in requested format:

```
close all
clear all

%% Calculating LAD
h = 6; %Height of coniferous Evergreen
z_m = 0.4*h; %Location at which maximum LAD occurs
LAI = 4; %Leaf Area Index
k = 50; %Number of discretizations


%Calculate L_m analytically
n = @(z) ((0≤z & z<z_m).*6 + (z_m≤z & z≤h)*0.5);
%n = @(z) ((0≤z & z<0.04*h).*6 + (0.04*h≤z & z<z_m).*0.5 + (z_m≤z & ...
    z≤h)*0.5); Modified interval of n

LAD = @(z,L_m) ...
    L_m.*((h-z_m)./(h-z)).^n(z).*exp(n(z).*(1-(h-z_m)./(h-z)));
f = @(L_m) integral(@(z)LAD(z,L_m),0,h,'waypoints',[0 z_m h])-LAI;
L_m = h*fzero(f,0);

%Use calculated L_m to discretize LAD
z = linspace(0,h,k);
LAD = L_m.*((h-z_m)./(h-z)).^n(z).*exp(n(z).*(1-(h-z_m)./(h-z)));
plot(LAD,z/h,'k')
axis([0 L_m*1.1 0 1])
xlabel('Leaf area density')
```

```
25 ylabel('Normalized canopy height (z/h)')
26
27
28 %% Specification blocks vegetation
29 Xstart_veg = 15;
30 Xend_veg = 27;
31 Ystart_veg = 0;
32 Yend_veg = 100;
33
34 X_s = ones(1,k-1)*Xstart_veg;
35 X_e = ones(1,k-1)*Xend_veg;
36 Y_s = ones(1,k-1)*Ystart_veg;
37 Y_e = ones(1,k-1)*Yend_veg;
38 Z_s = z(1:end-1); %Number of intervals are k-1
39 Z_e = z(2:end);
40
41 A = (LAD(1:end-1)+[LAD(2:end-1),LAD(end-1)])/2; %Taking average of ...
      LAD for each interval on z
42
43 Array_veg = round([X_s;X_e;Y_s;Y_e;Z_s;Z_e;A]',5);
44
45 for i = 1:size(Array_veg,1)
46     if Array_veg(i,7) == 0
47         fprintf('%1.0f. %1.0f. %1.0f. %1.0f. %1.1f %1.1f %1.0f. ...
              \n',Array_veg(i,:))
48     else
49         fprintf('%1.0f. %1.0f. %1.0f. %1.0f. %1.1f %1.1f %1.4f ...
              \n',Array_veg(i,:))
50     end
51 end
52
53 Table = array2table(Array_veg,'VariableNames',...
54 {'X_start','X_end','Y_start','Y_end','Z_start','Z_end','LAD'});
55
56
57 %% Specification blocks barrier
58 Xstart_block = 0;
59 Xend_block = 12;
60 Ystart_block = 0;
61 Yend_block = 100;
62 Zstart_block = 0;
63 Zend_block = 2;
64
65 Array_block = ...
      [Xstart_block;Xend_block;Ystart_block;Yend_block;Zstart_block;Zend_block]';
66
67 for i = 1:size(Array_block,1)
68         fprintf('%1.0f. %1.0f. %1.0f. %1.0f. %1.0f. %1.0f. ...
              \n',Array_block(i,:))
69 end
```